Supplementary Information: Outstanding nobility observed in Cu_5 clusters reveals the key role of collective quantum effects

David Buceta,[†] Shahana Huseyinova,[†] Miguel Cuerva,[†] Héctor Lozano,[†] Lisandro J. Giovanetti,[‡] José M. Ramallo-López,[‡] Patricia López-Caballero,[¶] Alexandre Zanchet,[¶,§] Alexander O. Mitrushchenkov,[‖] Andreas W. Hauser,[⊥] Giampaolo Barone,[#] Cristián Huck-Iriart,[@] Carlos Escudero,[△] Juan Carlos Hernández-Garrido,[▽] José Juan Calvino,[▽] Miguel López-Haro,[▽] María Pilar de Lara-Castells,[*,¶] Félix G. Requejo,[*,‡] and M. Arturo López-Quintela[*,†]

E-mail: Pilar.deLara.Castells@csic.es; requejo@inifta.unlp.edu.ar; malopez.quintela@usc.es

[*]To whom correspondence should be addressed

[†]Department of Physical Chemistry, Nanomag Laboratory, Universidad de Santiago de Compostela, E-15782 Santiago de Compostela, Spain.

[‡]Instituto de Investigaciones Fisicoquímicas Teóricas y Aplicadas (INIFTA), Dto. de Química, Facultad de Ciencias Exactas, UNLP and CONICET. Diag 113 y 64. 1900 La Plata, Argentina.

[¶]Instituto de Física Fundamental (AbinitSim Unit), CSIC, Serrano 123, 28006 Madrid, Spain.

[§]Dpto. de Química Física, Facultad de Química, Universidad de Salamanca, Salamanca, Spain.

[‖]MSME, Univ Gustave Eiffel, UPEC, CNRS, F-77454, Marne-la-Vallée, France.

[⊥]Graz University of Technology, Institute of Experimental Physics, Petersgasse 16, 8010 Graz, Austria.

[#]Department of Biological, Chemical and Pharmaceutical Sciences and Technologies, University of Palermo, 90128 Palermo, Italy.

[@]Laboratorio de Cristalografía Aplicada, Escuela de Ciencia y Tecnología, Universidad Nacional de San Martín (UNSAM), Campus Miguelete, 25 de Mayo y Francia, 1650 San Martín, Provincia Buenos Aires, Argentina.

[△]ALBA Synchrotron Light Source, Carrer de la Llum 2-26, 08290 Cerdanyola del Vallès, Barcelona, Spain.

[▽]Department of Material Science and Metallurgic Engineering and Inorganic Chemistry, Faculty of Science, University of Cádiz, Puerto Real (Cádiz), 11510 Spain.

Contents

Supplementary Section 1: Figures

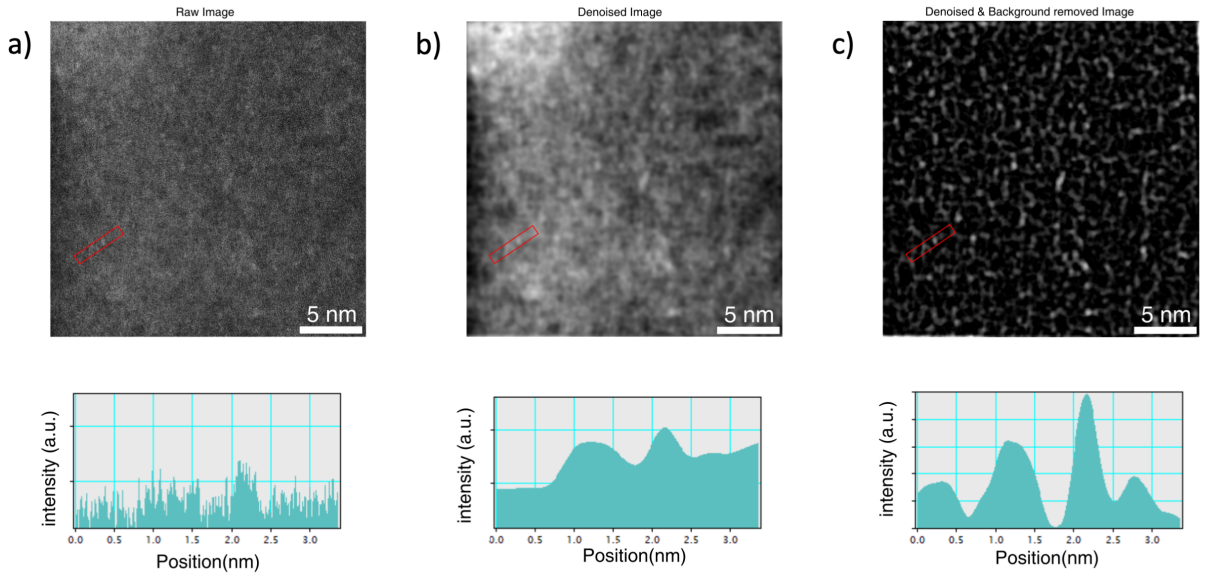

Supplementary Figure 1: **Schematic procedure for denoising of experimental HAADF-STEM images of the Cu_5 clusters. a,** Experimental AC HAADF-STEM image of the synthesized Cu_5 clusters. Intensity profiles, registered in a random area, illustrate the reduction of the noise within the background signals. **b,** Denoised image by combining Anscombe Variance Stabilization Transform (Anscombe VST) with the Undecimated Wavelet Transform (UWT). **c,** Background subtraction by disk tophat filtering.

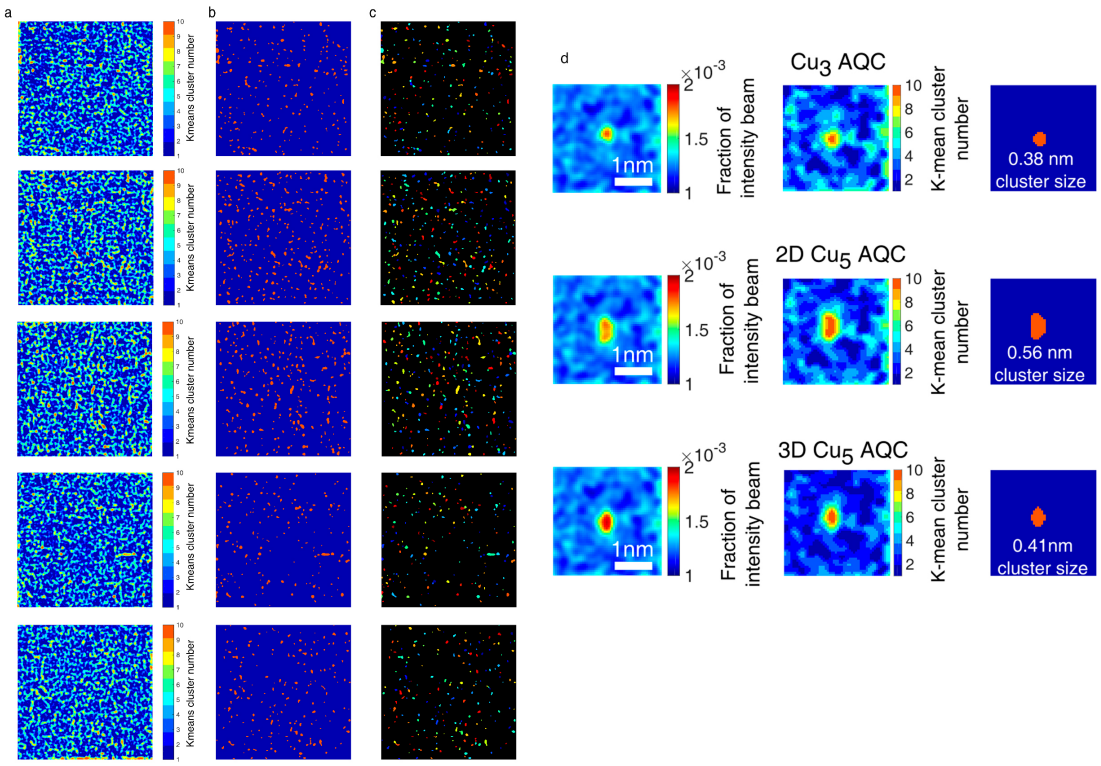

Supplementary Figure 2: **Analysis of AC HAADF-STEM images of Cu species by the *k*-means clustering method. a**, *k*-means clustering maps resulting from several raw images after denoising and background subtraction. **b**, Binarized images obtained from the *k*-means clustering analysis (Cu clusters in orange and background in blue). **c**, Pseudo-colour image after applying a watershed segmentation. Clusters with similar areas are displayed with the same colour. A total number of 1200 clusters were automatically detected and measured after clustering and segmentation. **d**, Characterization of modelled Cu clusters. Simulated HAADF-STEM images, after addition of Poisson and white Gaussian noise, from modelled Cu clusters with Cu_3-planar, Cu_5-planar (2D) and Cu_5-trigonal bipyramidal (3D) structures, respectively (left column). Results of the *k*-means cluster analysis from these modelled Cu_3-Cu_5 clusters and their segmentation by thresholding on binarized versions are also shown in the middle and right columns, respectively.

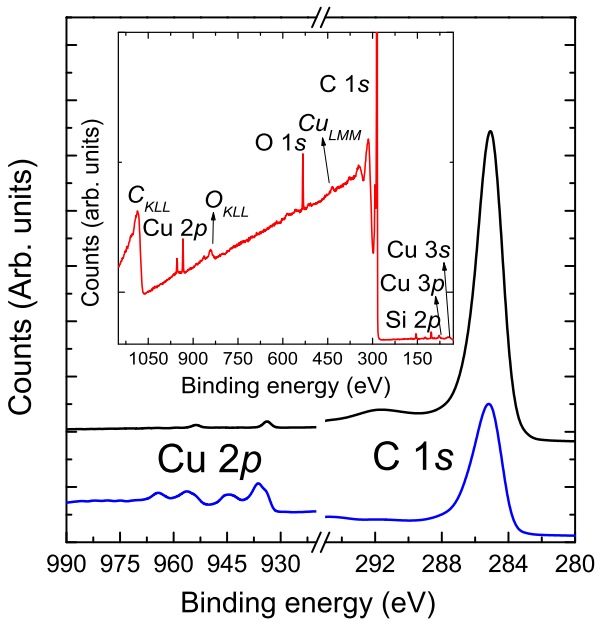

Supplementary Figure 3: **XPS spectra at the Cu 2*p* and C 1*s* levels for the "concentrated" and "monolayer" samples (shown with blue and black lines, respectively) taken from their respective surveys scans, as obtained in HV at RT with a incident photon energy of 1350 eV.** The x axis, indicating the binding energy, has been interrupted to better compare the regions associated to the Cu 2*p* and C 1*s* levels. The inset shows the complete XPS survey for the "monolayer" sample, where it is possible to notice the cleanliness of the sample. Only traces of Si are observed, which is a typical contaminant in HOPG substrates that do not interfere with the analysis carried out in this work.

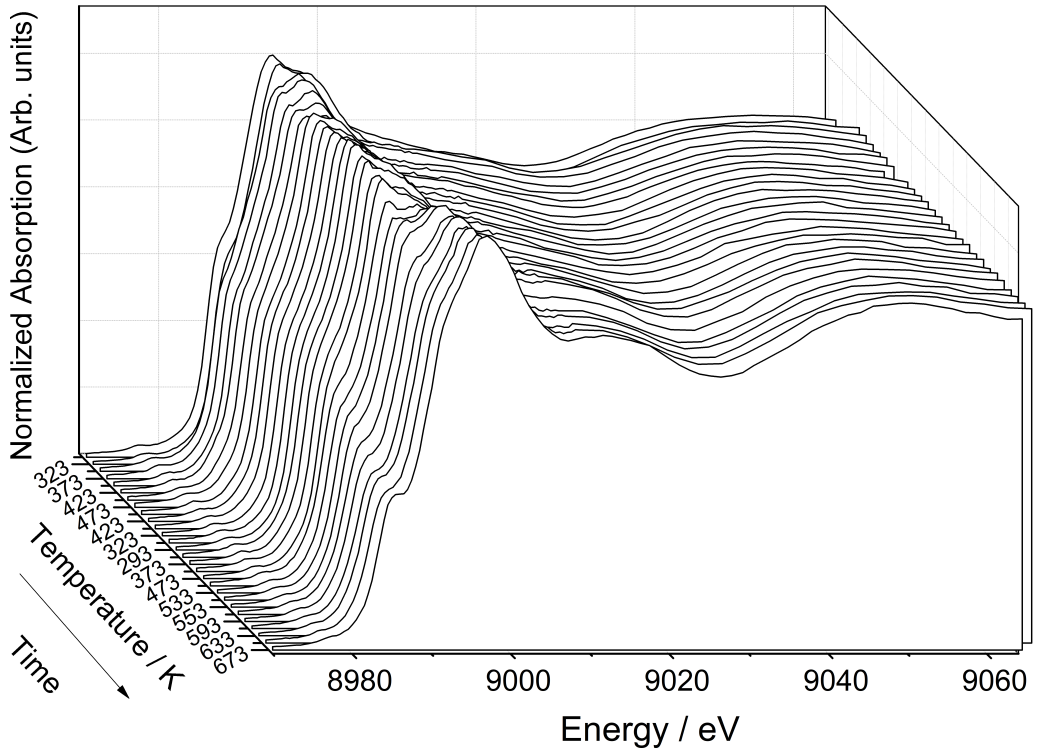

Supplementary Figure 4: **Cu K-edge XANES spectra of the Cu_5 clusters supported on HOPG obtained in air during the different cycles in the temperature range from RT to 673 K.**

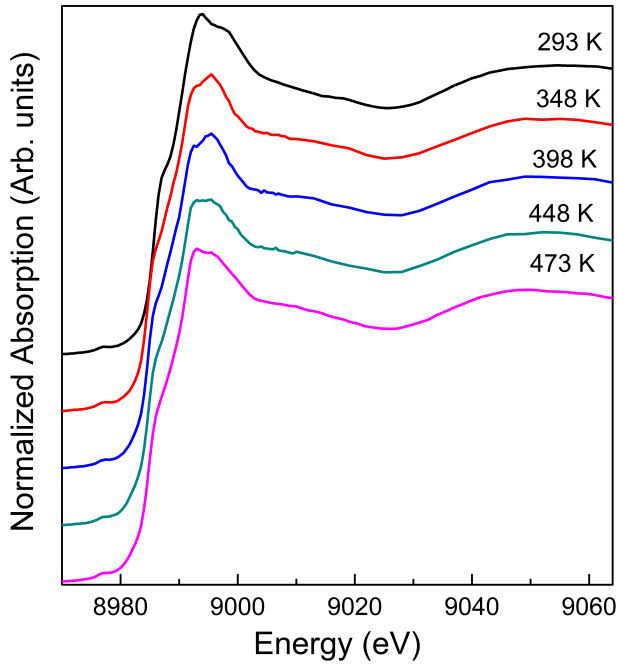

Supplementary Figure 5: **XANES spectra at the Cu K-edge of the Cu_5 clusters supported on HOPG**, as obtained in air from room temperature to 473 K during the first heating process. It is possible to observe slight differences between the spectra.

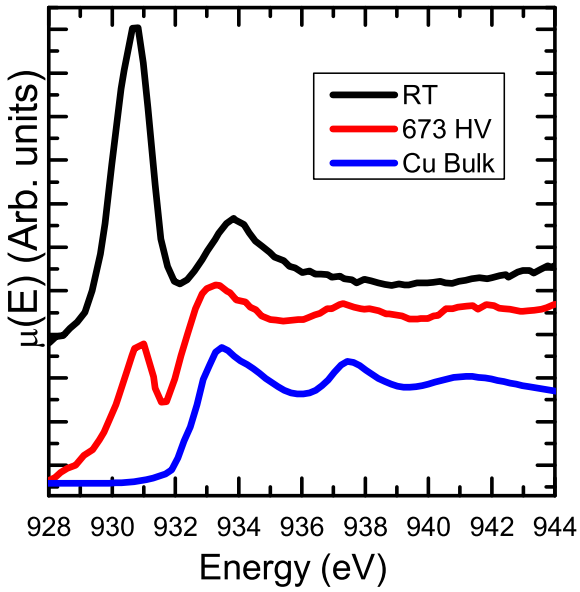

Supplementary Figure 6: **Cu L_3-edge XANES spectra of Cu_5 clusters on HOPG, with a similar Cu concentration to that used in the Cu K-edge XANES measurements.** Spectra were collected *in situ* at room temperature (black) and after being heated at 673 K (red) in HV. The spectrum of metallic Cu is shown for comparison (blue).

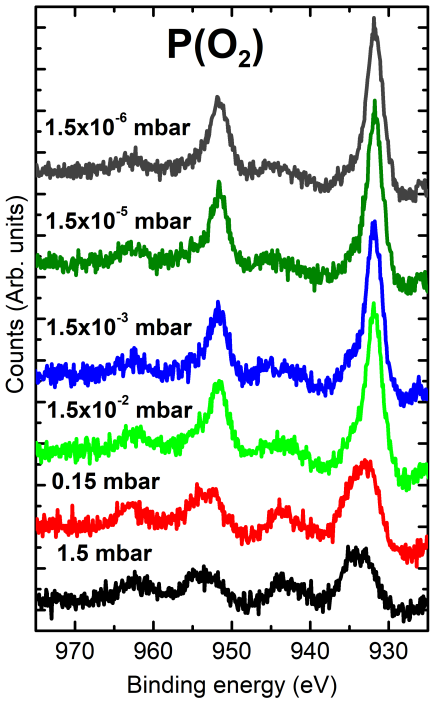

Supplementary Figure 7: **XPS spectra of Cu_5 clusters on HOPG at the Cu 2*p* photopeaks region.** All spectra were taken at room temperature at the indicated oxygen pressure.

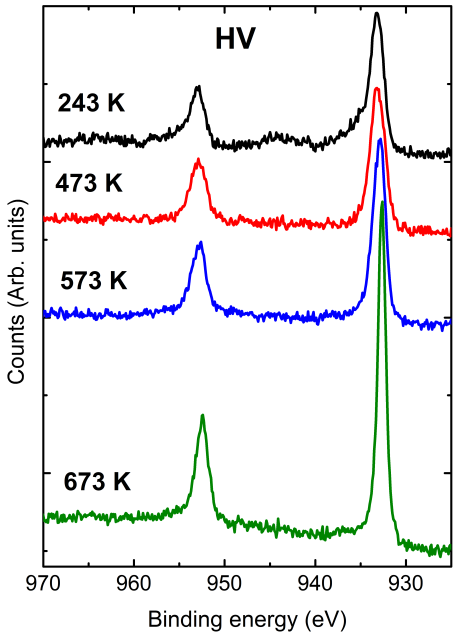

Supplementary Figure 8: **XPS spectra of Cu_5 clusters on HOPG at the Cu 2*p* photopeaks region.** All spectra were taken at the indicated temperatures and high vacuum (HV) after the sample preparation in air.

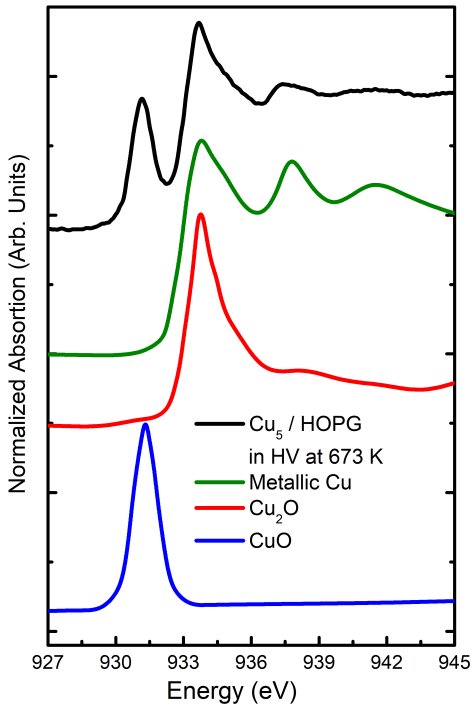

Supplementary Figure 9: **Cu L_3-edge XANES normalized spectra for metallic Cu, Cu_2O and CuO reference compounds together with that of Cu_5 clusters on HOPG sample in HV after heating in vacuum at 673 K.**

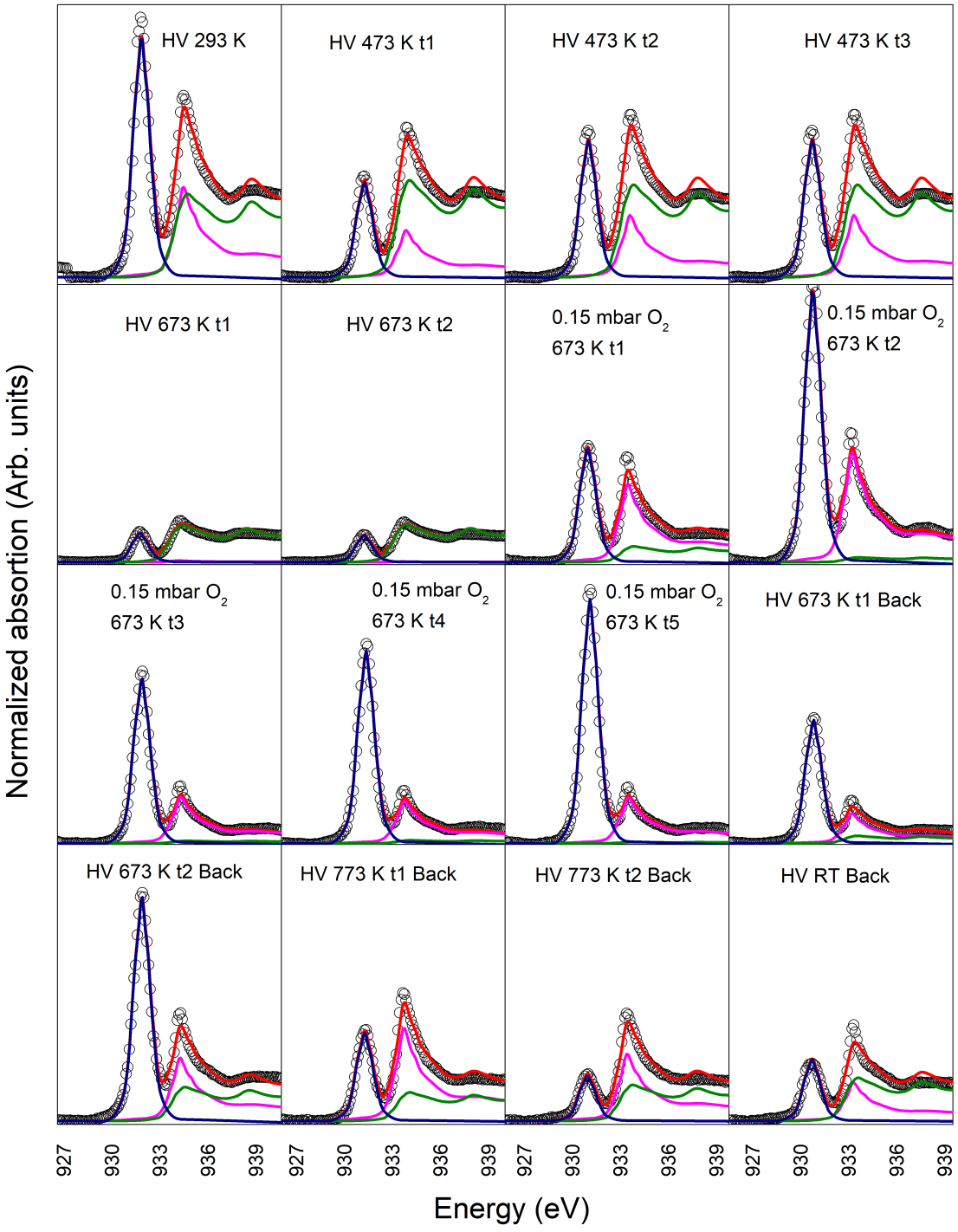

Supplementary Figure 10: **Linear combination fits of the Cu L_3-edge XANES spectra for all analyzed thermodynamic conditions.** Experimental data (open dots), linear combination fit (red line). CuO, Cu_2O and metallic Cu contributions are shown in blue, magenta and green lines, respectively.

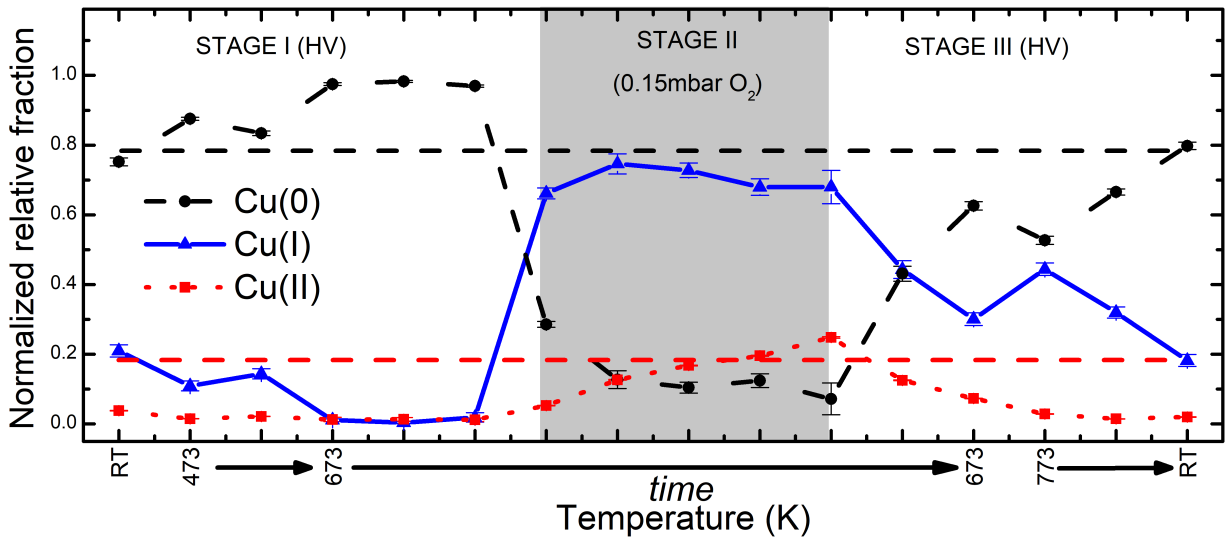

Supplementary Figure 11: **Relative fraction of Cu oxidation states in Cu_5 clusters through the different stages of a cycle carried out from RT changing temperature and oxygen pressure**. Horizontal dotted lines indicate the initial concentration of the Cu(0) and Cu(I) states (shown with black and red colors, respectively). Error bars indicate the uncertainty of the linear combination fit algorithms used for the fitting procedure.

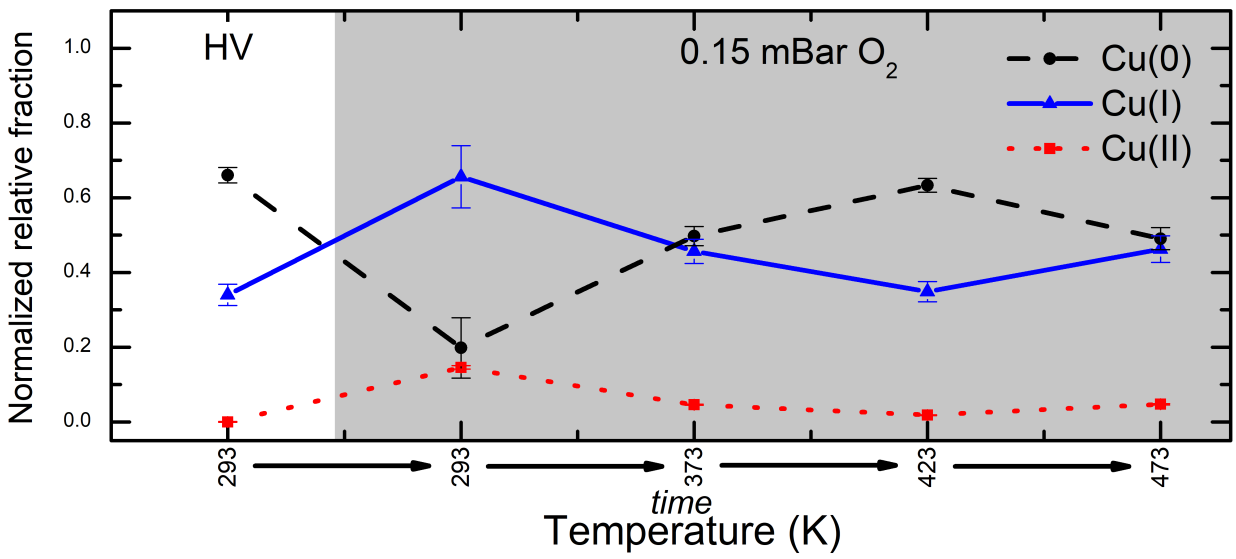

Supplementary Figure 12: **Relative fractions of Cu oxidation states upon oxidation/reduction cycling at low temperatures and oxygen pressure**. The initial state of the system corresponds to the supported Cu_5 clusters on HOPG in high vacuum (white region) after a degassing treatment to remove the hydration shell from the mother's solution. Error bars indicate the uncertainty of the linear combination fit algorithms used for the fitting procedure.

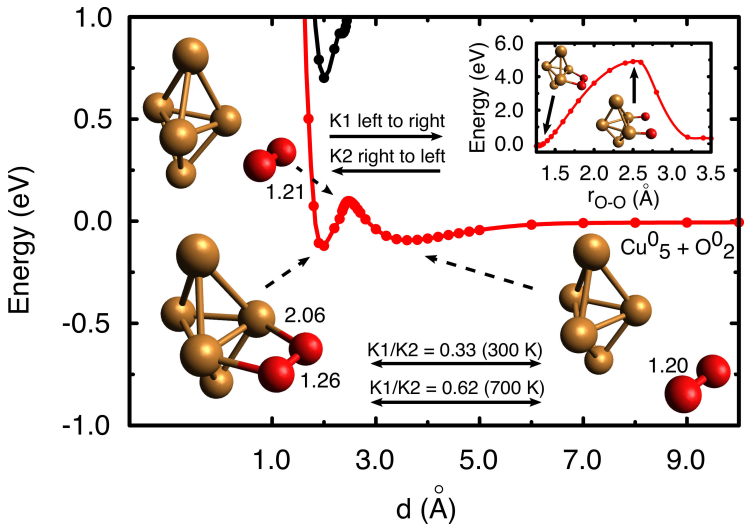

Supplementary Figure 13: **Reversible molecular oxidation of Cu_5–O_2.** Approximate O_2–Cu_5 reaction energy pathway in the adiabatic ground state (shown in red). The adiabatic excited state is shown in black. The geometries of the reactants are allowed to relax at each O_2–Cu_5 distance d. Estimates of the ratio of reaction rates from left to right (denoted as K_1) and right to left (referred to as K_2) are also shown at 300 and 700 K.

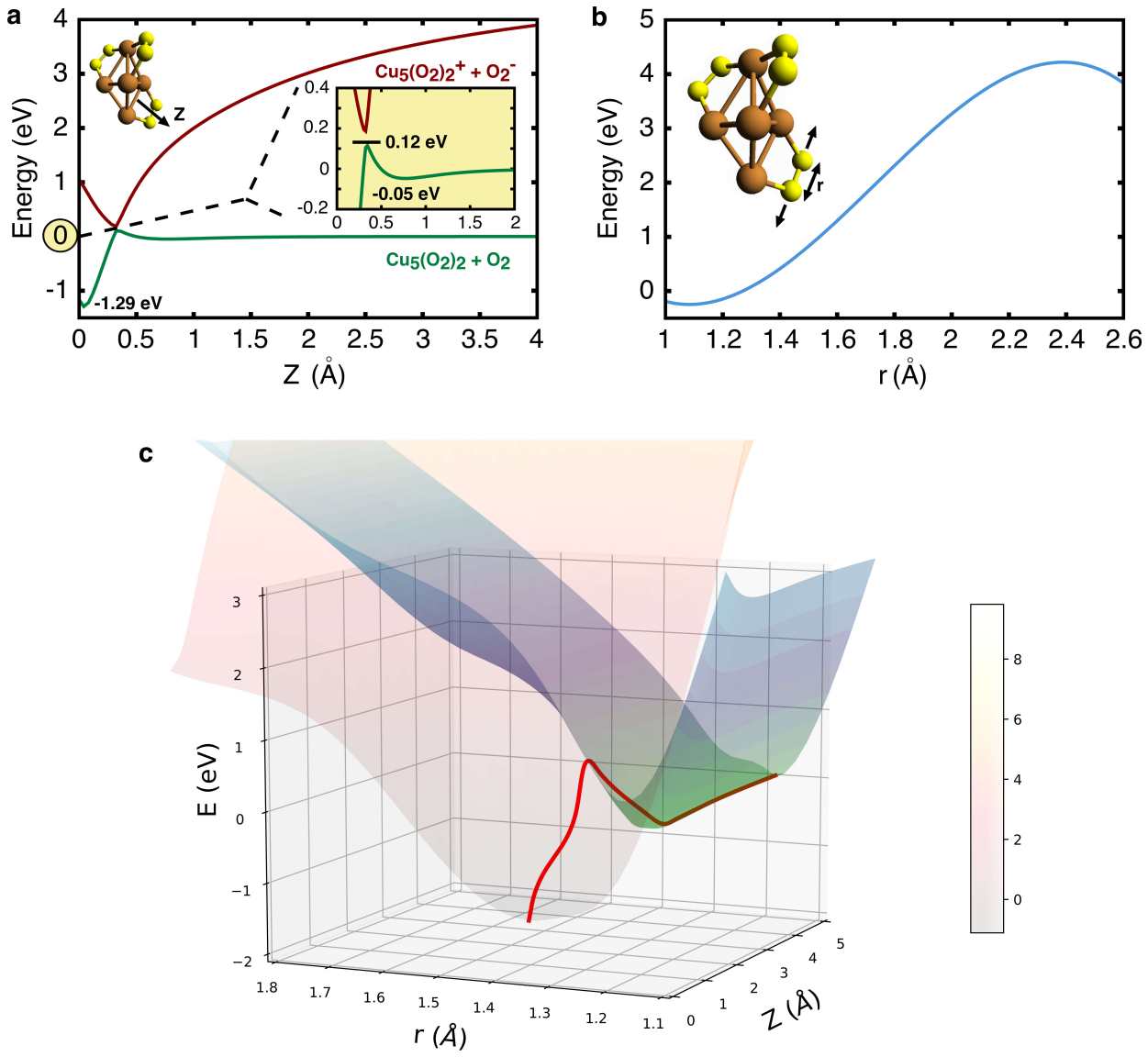

Supplementary Figure 14: **Reversible molecular oxidation of the $Cu_5(O_2)_2$–O_2 complex. a,** $Cu_5(O_2)_2$–O_2 reaction energy pathway in the adiabatic representation. In the reactants region, the neutral state (green) corresponds to the ground state and the ionic-pair state (red) corresponds to the excited state. In the chemisorption region, the ground state present ionic character while the neutral state lies higher in energy. For clarity, an expanded view of the region of the barrier is represented showing the avoided crossing between the two states. **b,** Potential energy scan providing the energy dependence upon the O–O stretching of one chemisorbed O_2 molecule, as located at the chemisorption well (see panel **a**). **c,** Two-dimensional (2D) representation of the potential energy surfaces, including the minimum energy pathway.

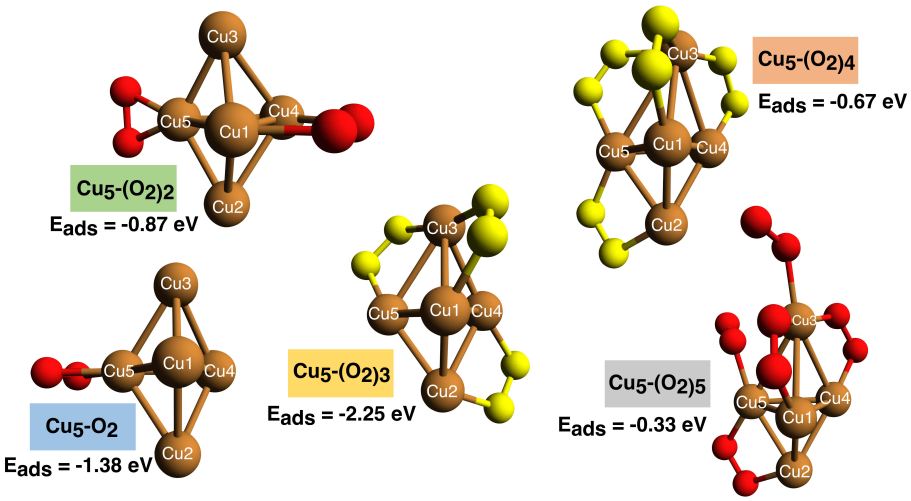

Oxidation state	Cu_5-O_2		Cu_5-$(O_2)_2$		Cu_5-$(O_2)_3$			Cu_5-$(O_2)_4$			Cu_5-$(O_2)_5$	
Level	DFT	HF	DFT	HF	DFT	HF	caspt2	DFT	HF	caspt2	DFT	HF
Cu1	0	0	+1	+1	+1	+1	+1/2	+3/4	+4/5	+4/5	+1	+1
Cu2	0	0	0	0	+1	+1	+1/2	+3/4	+4/5	+4/5	+1	+1
Cu3	0	0	0	0	+1	+1	+1	+2	+4/5	+4/5	+1	+1
Cu4	0	0	+1	+1	+1	+1	+1/2	+3/4	+4/5	+4/5	+1	+1
Cu5	+1	+1	+1	+1	+1	+1	+1/2	+3/4	+4/5	+4/5	+1	+1

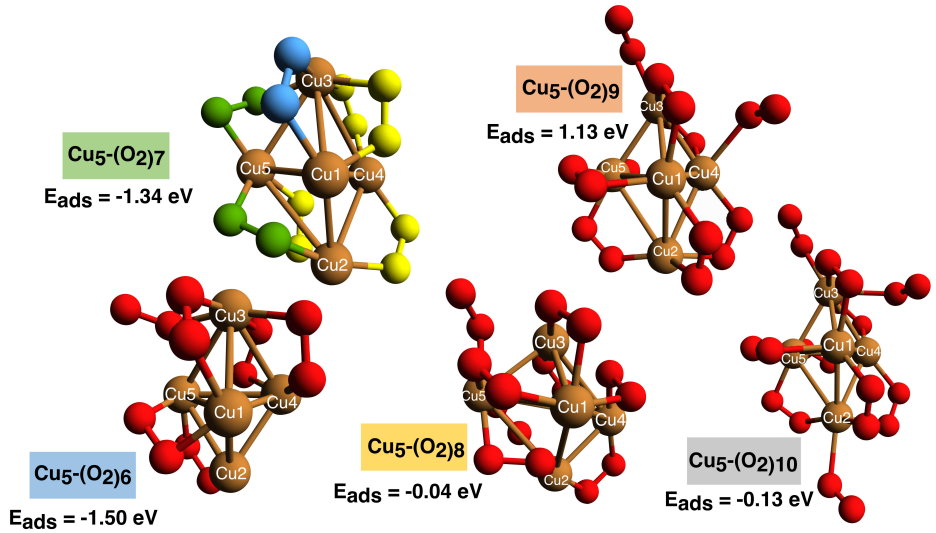

Oxidation state	Cu_5-$(O_2)_6$		Cu_5-$(O_2)_7$			Cu_5-$(O_2)_8$		Cu_5-$(O_2)_9$		Cu_5-$(O_2)_{10}$	
Level	DFT	HF	DFT	HF	caspt2	DFT	HF	DFT	HF	DFT	HF
Cu1	+2	+1	+1	+1	+1	+1	+2	+1	+1	+1	+1
Cu2	+1	+1	+2	+2	+2	+2	+2	+2	+1	+2	+1
Cu3	+2	+2	+2	+2	+2	+1	+1	+2	+1	+2	+1
Cu4	+2	+1	+2	+1	+1	+2	+2	+1	+1	+1	+1
Cu5	+2	+2	+2	+2	+2	+1	+2	+1	+1	+1	+1

Supplementary Figure 15: **Optimized structures, adsorption energies, and oxidation states of the copper atoms in Cu_5–$(O_2)_n$ complexes** ($n \leq 10$). Optimized stuctures and adsorption energies of Cu_5–$(O_2)_n$ complexes ($n \leq 10$), as calculated with the PBE-D3(BJ) approach and the def2-TZVP basis set. Assigned chemical oxidation states of copper atoms are also shown. The oxygen atoms colored in yellow, green, and blue highlight superoxo (O_2^-), peroxo (O_2^{2-}), and neutral O_2 species for the most stable complexes from the phase diagram (see Supplementary Section 14).

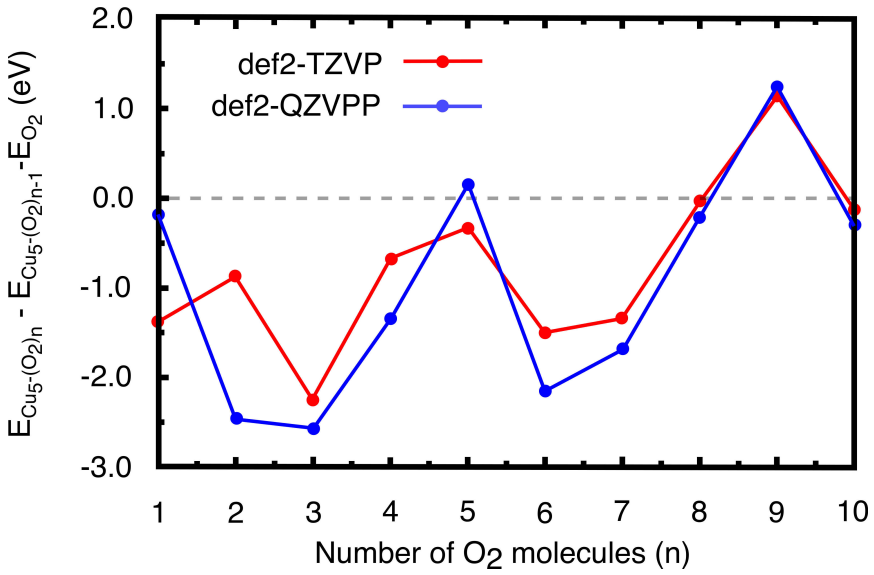

Supplementary Figure 16: **Adsorption energies as a function of the cluster size (n) for $(O_2)_n$–Cu_5 complexes.** Adsorption energies as a function of the cluster size (n) for $(O_2)_n$–Cu_5 complexes ($n \leq 10$), calculated at the PBE-D3(BJ) level of theory with the def2-TZVP (red) and the larger def2-QZVPP (blue) basis set.

a

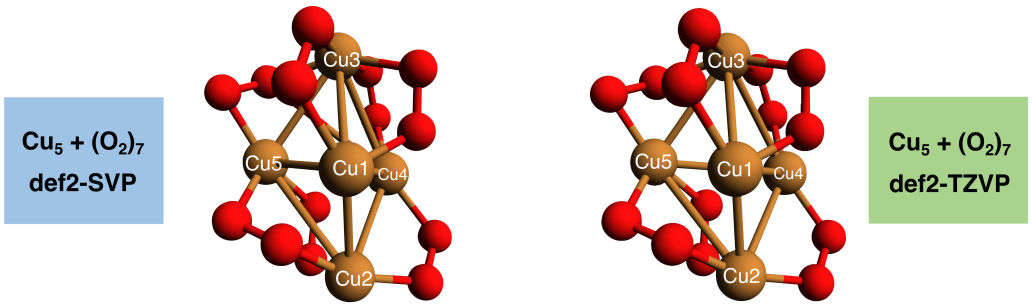

$Cu_5 + (O_2)_7$ def2-SVP

$Cu_5 + (O_2)_7$ def2-TZVP

Distance (Å)	$Cu_5 + (O_2)_7$ def2-SVP	$Cu_5 + (O_2)_7$ def2-TZVP
Cu1-Cu2	2.543	2.535
Cu1-Cu3	3.081	3.059
Cu1-Cu4	2.852	3.014
Cu1-Cu5	2.751	2.790
Cu2-Cu4	2.939	3.007
Cu2-Cu5	3.356	3.361
Cu3-Cu4	3.173	3.227
Cu3-Cu5	3.022	2.981
Cu4-Cu5	3.051	3.242

b

$Cu_5 + (O_2)_7$ no dispersion

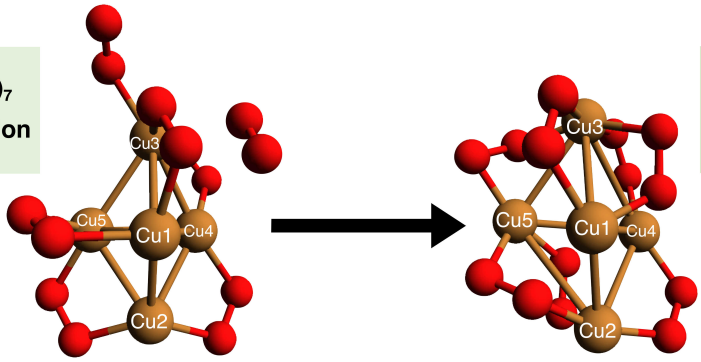

$Cu_5 + (O_2)_7$ dispersion

Distance (Å)	$Cu_5 + (O_2)_7$ no dispersion	$Cu_5 + (O_2)_7$ dispersion
Cu1-Cu2	2.552	2.535
Cu1-Cu3	2.827	3.059
Cu1-Cu4	2.566	3.014
Cu1-Cu5	2.483	2.790
Cu2-Cu4	2.512	3.007
Cu2-Cu5	2.594	3.361
Cu3-Cu4	2.573	3.227
Cu3-Cu5	2.686	2.981
Cu4-Cu5	2.612	3.242

Cu-Cu bond elongation

Supplementary Figure 17: **Convergence of structural parameters with the basis set size and effect of the dispersion interaction. a**, Comparison of the values of the Cu−Cu distances from the Cu_5–$(O_2)_7$ complex when calculated with the def2-SVP and def2-TZVP basis sets. **b**, Comparison of the values of the Cu−Cu distances from the Cu_5–$(O_2)_7$ complex when calculated without dispersion (left-hand structure) and adding the dispersion interaction (right-hand structure).

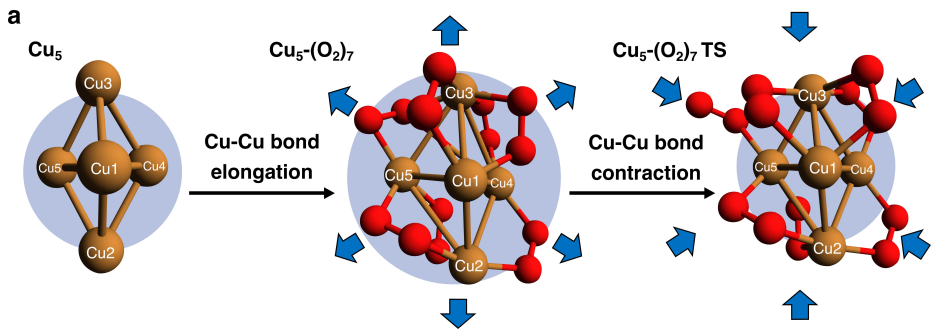

Distance (Å)	Cu_5	Cu_5-$(O_2)_7$	Cu_5-$(O_2)_7$ TS
Cu1-Cu2	2.455	2.535	2.491
Cu1-Cu3	2.458	3.059	2.731
Cu1-Cu4	2.352	3.014	2.560
Cu1-Cu5	2.564	2.790	2.660
Cu2-Cu4	2.440	3.007	2.577
Cu2-Cu5	2.456	3.361	2.934
Cu3-Cu4	2.439	3.227	2.682
Cu3-Cu5	2.456	2.981	2.550
Cu4-Cu5	2.361	3.242	2.604

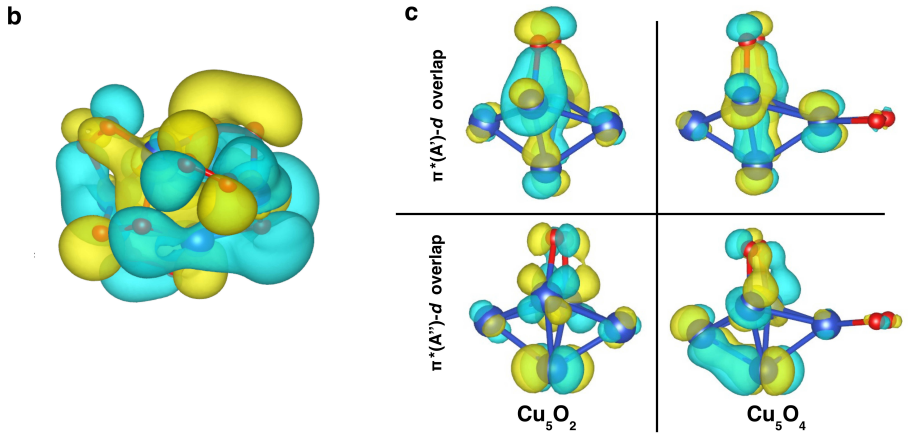

Supplementary Figure 18: **Collective effects in the adsorption of O_2 molecules to the Cu_5 cluster. a**, Figure showing how a Cu_5 cluster adsorbs and loses O_2 molecules by concerted elongations and contractions of Cu−Cu bonds. **b**, Picture of one occupied molecular orbital of the Cu_5–$(O_2)_7$ complex: the charge is collectively shared by the π^* orbitals of several O_2 molecules and collectively donated from $3d$ orbitals of most copper atoms. The pictured molecular orbital has significant projection on the $3d$ orbital of just one copper atom. **c**, Representative orbitals illustrating the nature of the $\pi^* - d$ bonding at the equatorial chemisorption (bridge) site in Cu_5–O_2 and Cu_5–$(O_2)_2$ complexes: the distortion of the $d-$orbitals arising from the absorption of a second oxygen molecule at the vortex site allows both $\pi^*(A')$ and $\pi^*(A'')$ orbitals of the equatorial O_2 molecule (the symmetric and anti-symmetric orbitals with respect to the equatorial plane of the cluster, respectively), to contribute to the bonding in the Cu_5–$(O_2)_2$ system. In contrast, the $\pi^*(A'')$ orbitals encompass negligible overlap with the $d-$orbitals from copper atoms in the Cu_5–O_2 complex. These orbitals have been obtained from *ab initio* calculations using multi-reference theory as described in Ref. 1.

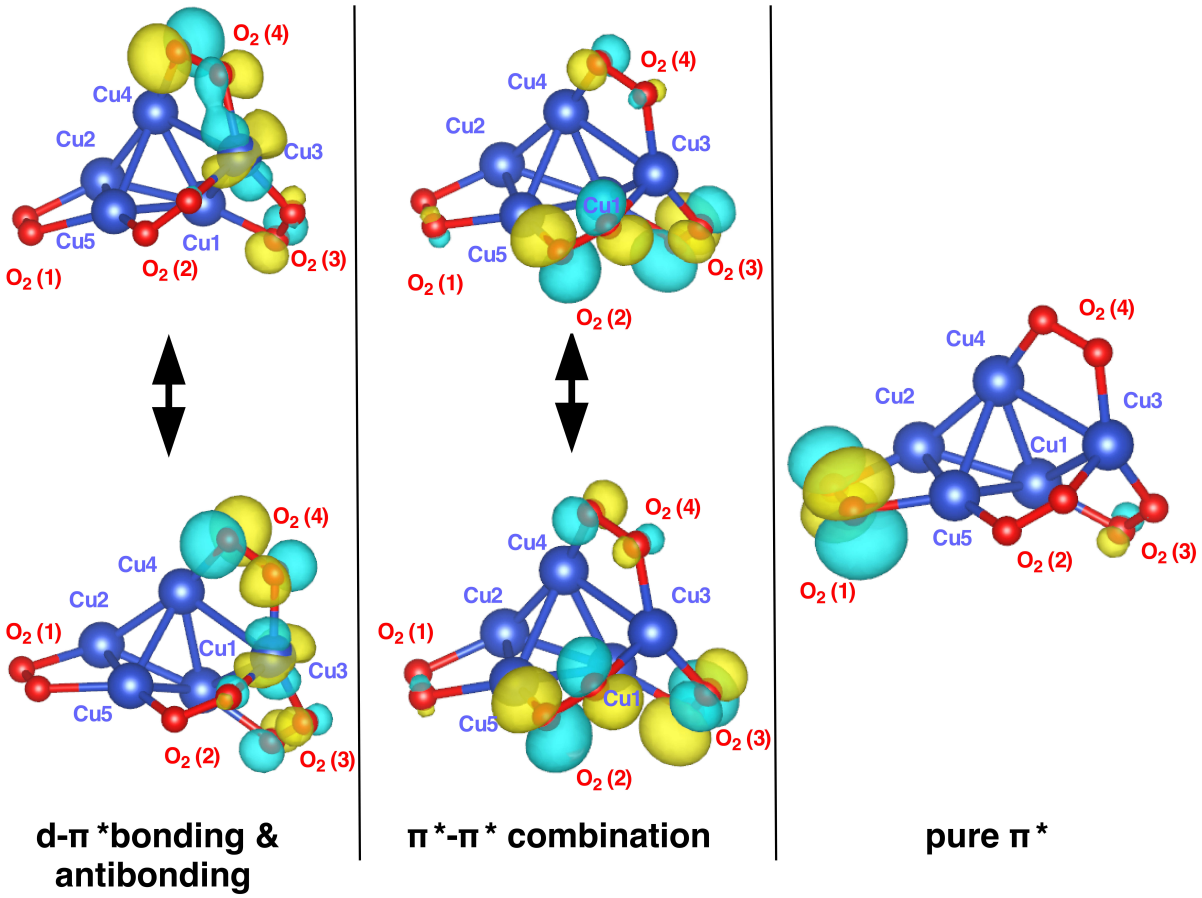

Supplementary Figure 19: **Characterization of the unpaired electrons of the Cu_5–$(O_2)_4$ complex.** Figure showing the five single-occupied orbitals of the Cu_5–$(O_2)_4$ system.

a

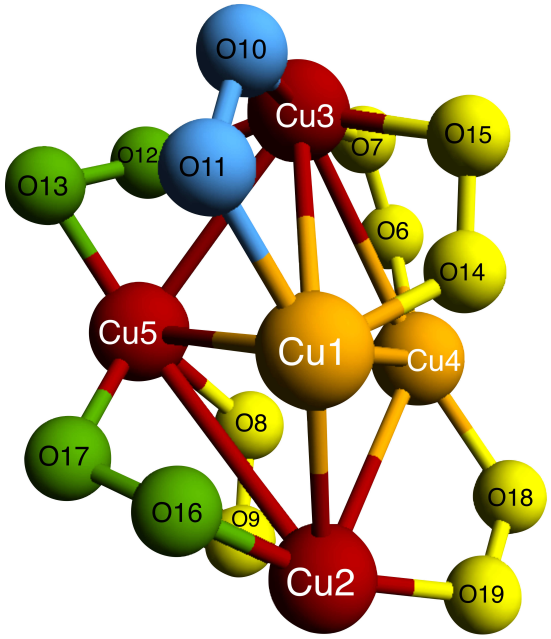

b

Cu atom	*s*	*p*	*d*	Oxidation state
Cu1	2.26	6.20	9.88	Cu(I)
Cu2	2.37	6.33	9.13	Cu(II)
Cu3	2.37	6.32	9.17	Cu(II)
Cu4	2.23	6.21	9.93	Cu(I)
Cu5	2.41	6.39	9.12	Cu(II)

c

O atom	*s*	*p*	*d*	Oxidation state
O6	3.88	4.25	0.05	superoxo
O7	3.87	4.50	0.04	
O8	3.89	4.59	0.04	superoxo
O9	3.91	4.15	0.04	
O10	3.90	4.10	0.04	neutral
O11	3.92	3.98	0.04	
O12	3.89	4.64	0.04	peroxo
O13	3.91	4.58	0.04	
O14	3.90	4.57	0.04	superoxo
O15	3.91	4.13	0.04	
O16	3.86	4.65	0.04	peroxo
O17	3.91	4.56	0.04	
O18	3.90	4.18	0.04	superoxo
O19	3.87	4.56	0.04	

Supplementary Figure 20: **Characterization of the oxidation states of Cu atoms from the Cu_5–$(O_2)_7$ complex**. **a**, Figure showing the structure of the Cu_5–$(O_2)_7$ complex and labelling of the different copper and oxygen atoms. Superoxo (O_2^-), peroxo (O_2^{2-}), and neutral O_2 molecules are represented with yellow, green, and blue balls, respectively. Copper atoms bearing Cu(II) and Cu(I) oxidation states are differentiated with red and brown colors. **b**, Mulliken population on atomic orbitals of copper atoms from the density matrix calculated for the Cu_5–$(O_2)_7$ complex using the CASPT2 method. The copper atoms are labelled as in Supplementary Figure 20a. **c**, Mulliken population on atomic orbitals of oxygen atoms from the density matrix calculated for the Cu_5–$(O_2)_7$ complex using the CASPT2 method. The oxygen atoms are labelled as in Supplementary Figure 20a.

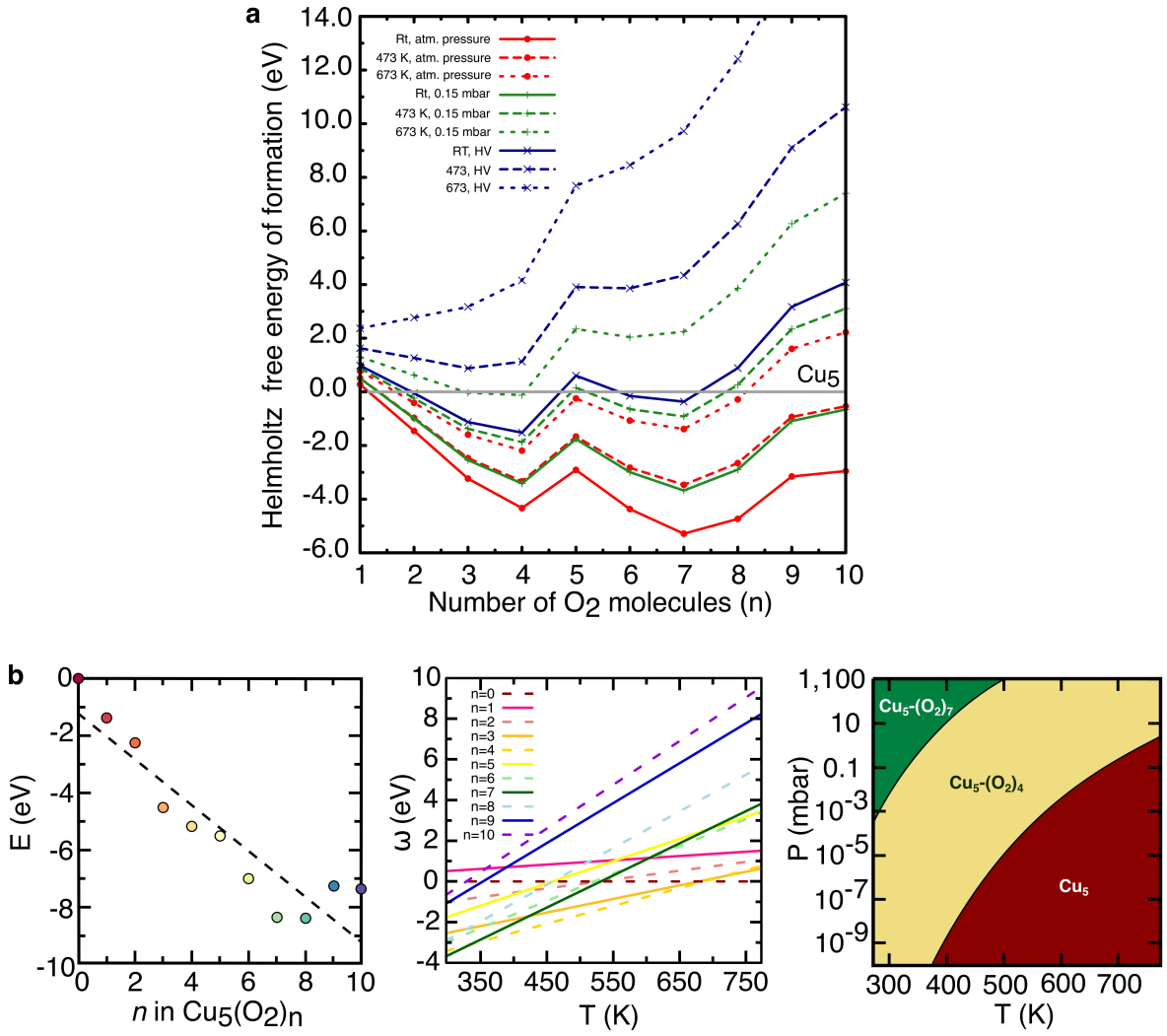

Supplementary Figure 21: **Helmholtz free energies of formation and phase diagram of Cu_5–$(O_2)_n$ complexes.** **a**, Free energies of formation of Cu_5–$(O_2)_n$ complexes, with the electronic energies and frequencies calculated using the def2-TZVP and def2-QZVPP basis sets, respectively, and the PBE-D3(BJ) approach. **b**, Left-hand panel: Electronic binding energies of the clusters as a function of the number of O_2 molecules. Middle panel: Free energy of formation (w potential) comparison at 0.15 mbar, with the color coding following dot colors in the left-hand panel. Even numbers of O_2 atoms are plotted as dashed lines. The predicted phases can be retrieved from the convex hull of the lowest energy curves. Right-hand panel: Final phase diagram, showing the most likely adsorption state as a function of pressure and temperature.

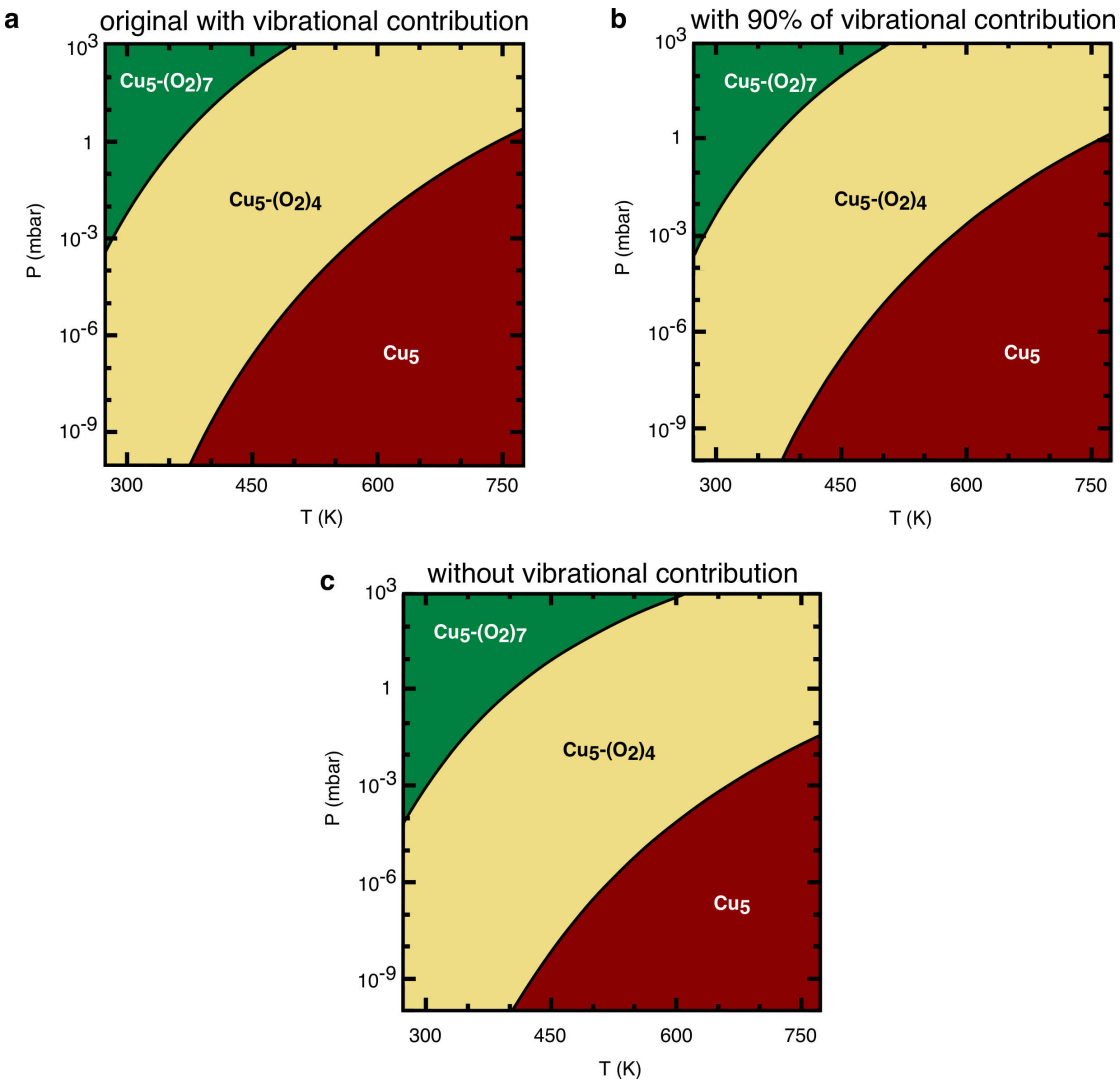

Supplementary Figure 22: **Phase diagrams as a function of the vibrational contributions.** **a**, Considering the vibrational terms **b**, Removing the 10% of the vibrational term, as an upper limit for the correction of the anharmonic contribution **c**, Without considering the vibrational terms.

a

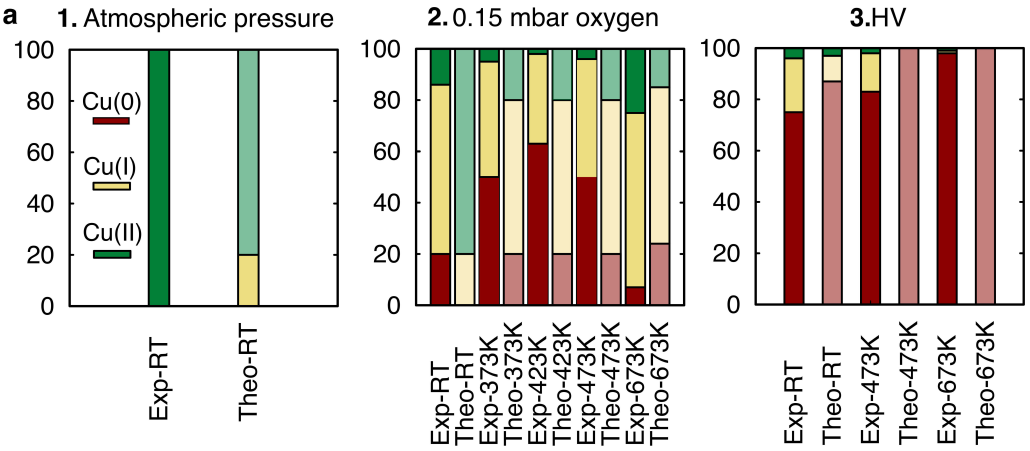

b

Method	%Cu(0)	%Cu(I)	%Cu(II)
Atmospheric pressure	**RT**		
Experimental (*)	0	0	100
Theory (*)	0	20	80
0.15 mbar oxygen	**RT**		
Experimental	20	66	14
Theory	0	20	80
	373 K		
Experimental	50	45	5
Theory	20	60	20
	423 K		
Experimental	63	35	2
Theory	20	60	20
	473 K		
Experimental	50	46	4
Theory	20	60	20
	673 K		
Experimental (t_f , last value)	7	68	25
Theory	24	61	15
High vacuum	**RT**		
Experimental	75	21	4
Theory (**)	87	10	3
	473 K		
Experimental	83	15	2
Theory	100	0	0
	673 K		
Experimental (t_f , last value) (***)	98	1	1
Theory	100	0	0

Supplementary Figure 23: **Comparison between theoretical and experimental results. a,** Chart diagram comparing the experimental and theoretical fractions at different values of the oxygen pressure and temperature. **b,** Summary of the estimated, experimental and theoretical, fractions of Cu(0), Cu(I), and Cu(II) states at different values of p and T. *The same experimental values are obtained from RT to 523 K while the theoretical values varied to within 3% only in between RT and 473 K. **Considering the probability of trapping at the physisorption state.[2] ***Fitted values before the oxygen treatment.

Supplementary Section 2: Tables

Supplementary Table 1: **Values obtained for the area under the Cu $2p_{3/2}$ and C 1*s* peaks, area ratio, atomic ratio, and thickness. These values have been calculated as described by Hill et al.[3]**

	Monolayer	Concentrated
Cu $2p_{3/2}$ Area (Arb. units)	677(3)	7589(9)
C 1*s* Area (Arb. units)	13000(10)	6675(8)
Cu/C Area ratio	0.052(5)	1.14(2)
Cu/C atomic ratio	0.16(2)	3.5(3)
Thickness (nm)	0.4(1)	4.3(2)

Supplementary Table 2: **Boltzmann-weighted averages of oxidation states (normalized fractions) at different values of temperature and oxygen pressure**. The averages have been calculated by applying the PBE-D3(BJ) approach with the def2-TZVP basis set for frequencies and the def2-QZVPP basis for electronic energies. The binding energies have been corrected for the basis set superposition error. Values between brackets have been obtained using the oxidation states estimated at *ab initio* (Hartree-Fock) level instead. At High-Vacuum (HV), the probability of trapping at the physisorption state has also been considered[2] (values between parenthesis).

Pressure	T	Cu(0)	Cu(I)	Cu(II)
1 atm	RT	0.0	0.20	0.80
		[0.0]	[0.40]	[0.60]
1 atm	473 K	0.01	0.22	0.77
		[0.01]	[0.42]	[0.57]
0.15 mbar	RT	0.0	0.20	0.80
		[0.0]	[0.40]	[0.60]
0.15 mbar	373 K	0.20	0.60	0.20
		[0.20]	[0.80]	[0.0]
0.15 mbar	423 K	0.20	0.60	0.20
		[0.20]	[0.80]	[0.0]
0.15 mbar	473 K	0.20	0.60	0.20
		[0.20]	[0.80]	[0.0]
0.15 mbar	673 K	0.24	0.61	0.15
		[0.31]	[0.69]	[0.0]
0.15 mbar	773 K	1.0	0.0	0.0
		[1.0]	[0.0]	[0.0]
HV	RT	0.20	0.60	0.20
		(0.87)	(0.10)	(0.03)
		[0.20]	[0.80]	[0.0]
		(0.87)	(0.13)	(0.0)
HV	473 K	1.0	0.0	0.0
		[1.0]	[0.0]	[0.0]
HV	673 K	1.0	0.0	0.0
		[1.0]	[0.0]	[0.0]
HV	773 K	1.0	0.0	0.0
		[1.0]	[0.0]	[0.0]

Supplementary Section 3: Advanced HAADF-STEM images processing

In order to improve the estimation of the size distribution of the Cu clusters, the binarized images have been processed by using morphological operations tools. In particular; i) objects smaller than 100 pixels were removed by an opening morphological operation; ii) features connected to the image edge were also eliminated using imclearborder, a pre-built matlab function; iii) the watershed transform method was used to separate connected objects after selecting cluster numbers from 8 to 10. This method is a well established image segmentation procedure applying region-based techniques. In particular, in this watershed segmentation analysis, the distance transform was applied.[4] It should be highlighted that using this methodology we avoid an overestimation of both smallest and largest clusters, which would lead to an incorrect size distribution.

Supplementary Section 4: XPS quantification of Cu_5 clusters deposited on HOPG

Aimed to compare different final concentrations of Cu_5 clusters deposited on HOPG, we estimated the Cu to C atomic ratio by using the XPS survey spectra of the samples under study (see Supplementary Figure 3). Due to the possible carbon contamination, the resulting estimate of the Cu to C atomic ratio could be undervalued. Yet, the carbon contamination signal could be safely discarded when it was compared to that of pure carbon in HOPG. The intensity of the Cu $2p_{3/2}$ and C $1s$ levels in these spectra was determined by integration once the background was properly subtracted (see Supplementary Table 1).

Just by comparing the ratio between the Cu $2p_{3/2}$ and C $1s$ intensities for each sample, it is possible to determine that the sample referred to as "concentrated" (used in the Cu K-edge XANES and NAP-XPS experiments) has a Cu_5 clusters concentration $\sim$ 20 times larger than the

so-named "monolayer" sample. These intensities were corrected by the proper relative sensitivity factor (RSF) in order to take into account the electron mean free path, cross section, and other experimental factors which are usually included to precisely estimate the atomic concentration by XPS.[5] These corrections allows to determine the copper to carbon atomic ratio summarized in Supplementary Table 1.

Using the intensities corrected by the RSF factors, it is possible to estimate the thickness of the Cu overlayer (see Supplementary Table 1).[3] This estimation, besides its simplicity, provides us with a raw estimation of the number of layers in each sample, being close to 1 for the "monolayer" sample and about 10 for the "concentrated" one. To get these values, it was assumed that the Cu_5 clusters size is that estimated by HAADF-STEM (approximately 0.4 nm), also described in the theoretical section.

Supplementary Section 5: Cu *K*-edge XANES experiments in air (high concentration of Cu_5 clusters)

Supplementary Figure 4 shows the complete set of Cu *K*-edge XANES spectra of Cu_5 clusters deposited on HOPG, measured at air and obtained with the following sequence: heating the sample from room temperature (RT) up to 473 K, cooling down to RT and then heating up to 673 K. All spectra exhibit the characteristic features of Cu atoms in the Cu(II) state, with the energy edge position at 8986 eV and a weak feature (pre-peak) located at 8979 eV.Supplementary Figure 5 shows the XANES spectra during the first heating process between RT and 473 K. Some changes are observed during this first stage. The most important one takes place at around 348 K, a temperature at which the edge position is slightly shifted by 1 eV towards lower energies. This shift is usually a consequence of the reduction of the Cu average oxidation state. However, Zhang et al.[6] have shown that a decrease in the coordination number under absorption of H_2O on Cu(II) causes a small shift to lower energies of the edge and changes in the feature at 8986 eV. Thus, the modifications observed in the XANES spectra during heating from RT to 348 K must be attributed not

to a change in the oxidation state but to the desorption of the hydration shell from mother solution and/or oxygen (degassing) during this first treatment.

XANES measurements at the Cu K-edge in air have shown that when the concentration of Cu_5 clusters on the HOPG surface is high (about ten monolayers according to the XPS experimental estimations, see Supplementary Figure 3), their Cu_5 clusters identity is lost due to the formation of bulk CuO when the temperature is increased above 673 K. To confirm this result, we performed a similar XANES measurement at the Cu L_3-edge in HV. Supplementary Figure 6 shows the XANES spectra of the Cu_5 clusters on HOPG in HV at RT and 673 K. The spectrum of bulk Cu is shown for comparison. It can be seen that at 673 K two oscillations appear at 637 and 641 eV, resembling those of bulk Cu, indicating the clusters coalescence. This confirms that the clusters stability is not related to the oxygen pressure but it is associated to the mobility of the clusters due to the temperature increase, taking place both in air and in HV conditions.

Supplementary Section 6: Near Ambient Pressure XPS experiments at different oxygen pressures

Cu 2p XPS spectra were taken at different pressures of oxygen at the Near Ambient Pressure XPS (NAP-XPS) main chamber. The purpose of these measurements was to identify the best choice of pressure for detecting oxidized Cu species without a significant signal attenuation due to the presence of the gas phase. Supplementary Figure 7 shows the corresponding Cu 2p XPS spectra for oxygen pressures in the range from 1.5×10^{-6} mbar to 1.5 mbar. Clearly, a pressure of the order of 0.15 mbar is high enough to form and detect the presence of oxidized Cu(II) species.

Supplementary Section 7: Cu 2*p* XPS experiments in HV (high concentration of Cu_5 clusters)

Supplementary Figure 8 shows the XPS spectra of Cu_5 clusters deposited on HOPG measured at HV. Before any heating treatment, the spectrum shows a small satellite and broad photopeaks, indicating the presence of the oxidized Cu(II) state. The fraction of non metallic Cu is certainly due to the manipulation of the sample in air before mounting it at the main chamber of the analyzer. During this first cycle, from 473 K up to 673 K, the spectra only shows the presence of the Cu(0) state. It indicates the removal of the O_2 molecules and/or hydration shell from the Cu_5 clusters just by heating to 473 K in HV, as was observed also during the first treatment at ambient pressure by XANES at the Cu *K*-edge (see Supplementary Figure 5).

Supplementary Section 8: Cu L_3-edge XANES experiments at high vacuum and 0.15 mbar of oxygen (low concentration of Cu_5 clusters)

Cu L_3-edge XANES measurements were performed on monolayer-like samples of Cu_5 clusters on HOPG. For these experiments, the temperature was varied between 293 K (RT) and 773 K, at high-vacuum (HV) and 0.15 mbar of oxygen pressure. In order to identify and quantify the different oxidation states and their relative concentration in the sample at different thermodynamic conditions, a linear combination fit of these XANES spectra was performed, following the procedure described by Eren et al.[7] Spectra of metallic Cu, Cu_2O and CuO were used as reference for Cu(0), Cu(I) and Cu(II) oxidation states, using the reported values of the Cu L_3-edge energies of 933.7, 933.7, and 931.3 eV, respectively.[8] Supplementary Figure 9 shows the Cu L_3-edge XANES spectra for the three reference compounds together with that of the Cu_5 clusters on HOPG sample in HV after heating in vacuum at 673 K. CuO and Cu_2O have strong absorption edges at 931.3

and 933.7 eV, respectively, and substantial shape differences between them and the corresponding spectrum of metallic Cu.

All the Cu L_3-edge XANES spectra collected at the different thermodynamic conditions and their corresponding fits are presented in Supplementary Figure 10. Finally, Supplementary Figure 11 shows the relative fractions of oxidation states of Cu atoms in Cu_5 clusters through the different stages of a cycle carried out from RT to 773 K at HV and 0.15 mbar of oxygen pressure (see Figure 3).

Aimed to reexamine and quantify the observed interaction between (molecular) oxygen and Cu_5 clusters by NAP-XPS, we performed Cu L_3-edge XANES experiments, fixing the oxygen pressure at 0.15 mbar, between RT and 473 K. This way, we confirmed that the Cu_5 clusters are reduced, even in the presence of (0.15 mbar) of oxygen. As aforementioned (see Figure 2c), the oxidation state reduction of Cu_5 clusters proceeds at moderated temperatures (in the range from 373 to 473 K) in presence of oxygen. The analysis of these measurements, shown in Supplementary Figure 11, not only corroborates the previous findings by NAP-XPS but also allows a "quantification" of the reduction mechanism. This way, the determined fractions of Cu oxidation states can be directly compared with the theoretical predictions in a wider range of thermodynamic parameters (see Supplementary Figure 23). The key result is a clear confirmation of the reduction of the oxidation state of the Cu_5 clusters in presence of 0.15 mbar of oxygen, after having been oxidized at RT under the same atmosphere.

Supplementary Section 9: Methods used in the theory part

In all calculations on bare Cu_5 clusters, a trigonal bipyramidal (3D) structure is assumed. Although the experimental measurements have been realized for Cu_5 clusters supported on highly oriented pyrolytic graphite (HOPG), a previous work[9] has shown that a Cu_5 cluster is only minimally perturbed when supported on a carbon-based surface (graphene) due to the dispersion-dominated nature of the Cu_5–graphene interaction. Specifically, using a dispersion-corrected DFT approach[10,11]

with the computational setup reported in Refs. 12,13 to describe the Cu_5/graphene interaction,[9] it was found from a Bader decomposition analysis[14] that the net charge donation from the copper cluster to the support is insignificant (less than 0.02 $|e|$). Therefore, the experimental results for HOPG-supported Cu_5 clusters are considered as representative of unsupported Cu_5 clusters.

Density functional theory (DFT) as well as multi-reference perturbation theory[15] have been applied to study the chemisorption of up to 10 O_2 molecules on Cu_5 clusters. To this end, we have employed a dispersion-corrected DFT-D3 ansatz,[10,11] given its well-proven performance in describing the adsorption of small silver clusters on a titanium dioxide (TiO_2) surface[16,17] and the optical properties of the same surfaces when modified via deposition of Cu_5 clusters.[9] Specifically, structural optimizations and the calculation of interaction energies have been performed with the Perdew-Burke-Ernzerhof (PBE) density functional and the Becke-Johnson (BJ) damping[10] for the D3 dispersion correction. This combination will be referred to as the PBE-D3(BJ) scheme. These calculations have been performed with the `ORCA`[18] suite of programs (version 4.0.1.2). The optimization of the geometries of the Cu_5– $(O_2)_n$ complexes have been accomplished using the atom-centered def2-TZVP[19] basis set for copper and oxygen atoms. Additional single-point calculations were carried out using the def2-QZVPP basis set.[19] The counterpoise method was employed to estimate the basis set superposition error.[20] Single-point calculations have been also performed at Møller-Plesset perturbation theory (MP2) level with the def2-SVP[19] basis set, and at Hartree-Fock (HF) level using the def2-TZVP[19] basis set. All the DFT calculations were carried out considering the doublet spin states of the Cu_5–$(O_2)_n$ complexes.

We have also applied multi-state complete-active-space second-order perturbation theory (MS-CASPT2). Two (doublet and quartet) spin states have been considered for a maximum number of seven adsorbed O_2 molecules. The validation of the DFT ansatz by a multi-reference method was mandatory due to the open-shell nature of the interacting species, allowing to account for the multi-reference character of the wavefunctions in ensuring the nature of the oxidation states of the copper atoms.

Multi-reference perturbation theory has been also applied to estimate the reaction pathway of

a single O_2 molecule interacting with the $Cu_5(O_2)_2$ complex, i.e., the Cu_5 clusters bearing two adsorbed O_2 molecules. As highlighted in Ref. 1, the application of a multi-reference method is inevitable since the wavefunction at the energy barrier between chemisorption and physisorption minima shows a strong multiconfigurational character, bearing a mixing of neutral and ionic contributions. We have considered the electronic state correlating with the neutral O_2 and $Cu_5(O_2)_2$ fragments in the asymptotic region (referred as the neutral state) and that correlating with the ionic O_2^- and $(Cu_5(O_2)_2)^+$ systems (referred as the ionic state). The ionic state, which is the ground state at the chemisorption minimum, is characterized by the strong Coulomb interaction between a negatively charged superoxo O_2^- radical and a positively charged $(Cu_5(O_2)_2)^+$ system and is asymptotically correlated to a separation in charged fragments O_2^- and $(Cu_5(O_2)_2)^+$. In contrast, the neutral state corresponds to the interaction between neutral fragments, and leads to a separation into O_2 and $Cu_5(O_2)_2$. This state is the ground state at the physisorption minimum.

The initial structure for the chemisorption state of the $Cu_5(O_2)_3$ complex has been the minimum energy geometry obtained at DFT-D3 level. The internuclear O–O distance has been found to differ significantly in neutral and ionic states at the corresponding physisorption and molecular chemisorption energy minima. Therefore, to get a good estimation of the actual reaction pathway, we have performed a two-dimensional (2D) scan: the first coordinate (Z) is the distance of the oxygen molecule (its center-of-mass) to the cluster, with $Z = 0$ defined as its optimized position in the chemisorption minimum of the $Cu_5(O_2)_3$ complex. The second coordinate is the inter-nuclear $O-O$ distance (R). We have applied the single-reference internally-contracted RS2C method[15] with density fitting (DF-RS2C), as implemented within the `MOLPRO` program package.[21] For this purpose, following the methodological strategy proposed in Refs. 22 and 23 to characterize the interaction of O_2 molecules with reduced TiO_2 surfaces, we first optimized the orbitals using the single-state DF-CASSCF method separately for neutral and ionic states, which allows to calculate directly diabatic states. This is possible if the `SUPER-CI` optimization method[24] is used as implemented in a recent version of the `MOLPRO` code.[25] Next, the single-reference RS2C method was applied to grasp dynamical correlation effects. Since the two diabatic states can cross, in the

2D representation depending on (R, Z) it is easy to locate the seam corresponding to the crossing of the neutral and the ionic state. The location of the transition state between physisorption and chemisorption states corresponds to the minimum energy crossing point (MECP) between the two diabatic states, being thus given by the position (Z, r) of the minimum of the seam.

The details of DF-CASSCF/DF-RS2C calculations are as follows: we used the polarized correlation-consistent triple-ζ basis of Dunning and collaborators[26] (cc-pVTZ) for oxygen atoms, and the cc-pVTZ-PP basis set for copper atoms[27] including a small (10-valence-electron) relativistic pseudopotential. For density fitting, the associated `MP2FIT` and `JKFIT` bases were used in CASSCF and RS2C calculations correspondingly. The active space was built from 7 electrons in 7 orbitals, while 68 closed-shell orbitals were fully optimized at the DF-CASSCF level. Of these, 32 core orbitals were not correlated at DF-RS2C level. Similarly to the case of the O_2–TiO_2 interaction (see Ref. 23), calculated neutral and ionic states are effectively “diabatic" but non-orthogonal states. To estimate the overlap and the non-adiabatic couplings, a bi-orthogonal approach, as implemented at CASSCF level in `MOLPRO` (see also Refs. 22,23,28,29), was applied at the geometry of the transition state.

Supplementary Section 9.1 Landau-Zener Model

To estimate the electron hopping probability between the diabatic electronic states of the $Cu_5(O_2)_2$–O_2 complex correlating with neutral and ionic fragments, we apply the Landau-Zener (LZ) model.[29–31] Within the LZ model, the electron hopping probability can be defined as $1 - P_{\mathrm{LZ}}$, with P_{LZ} being the LZ probability for a non-adiabatic transition:

$$P_{\mathrm{LZ}}(v) \approx exp[(-2\,\pi\,\mathrm{H}_{12}^2)/(F_{12}\,v)]. \tag{S1}$$

In the above expression, v is the relative velocity of the fragments, F_{12} is the difference between the two slopes F_1 and F_2 of the diabatic potential energy surfaces at the intersection between the neutral and ionic states, and H_{12} is the off-diagonal matrix element of the electronic Hamiltonian.

Assuming a Maxwell-Boltzmann (MB) distribution for the relative velocities of the reactants, the electron hopping probability can be written as a function of temperature. For this purpose, we integrate over the hopping probabilities from the LZ model, P_{LZ}, expressed as a function of the velocity v in the reaction coordinate (i.e., defining the minimum energy pathway), and weighted with a Boltzmann factor P_{MB},

$$P_{\mathrm{LZ}}(T) \approx \int dv\, P_{\mathrm{LZ}}(v) \times P_{\mathrm{MB}}(v) \tag{S2}$$

where $P_{\mathrm{MB}}(v)$ denotes the MB distribution of relative velocities in one direction,

$$P_{\mathrm{MB}}(v) = \left(\frac{\mu}{2\pi k_{\mathrm{B}} T}\right)^{1/2} e^{-\mu\, v^2/2k_{\mathrm{B}}T} \tag{S3}$$

with k_{B} as the Boltzmann constant.

Supplementary Section 10: Reversible molecular oxidation of Cu_5–O_2

Ref. 1, a theoretical study based on multi-reference perturbation theory, explains the resistivity of the Cu_5 cluster with respect to an “irreversible" oxidation by a single O_2 molecule in detail. For this purpose, the reaction barrier shown in Supplementary Figure 13 was interpreted as an avoided crossing of the ground state, shown in red and asymptotically correlated with the neutral reactants, and an excited state, shown in black and asymptotically correlated with the ionic O_2^- and Cu_5^+ species. Note that the electronic configuration of the adiabatic ground state changes in the vicinity of the avoided crossing. While passing the resulting transition state barrier this configuration changes its character from neutral to ionic (two reaction fragments of opposite sign). However, since this process is not happening infinitely slowly, there is a certain probability for the system to remain in its former electronic configuration. This type of transition dynamics is also covered by Landau-Zener theory (see Supplementary Section 9.1), which allowed us to estimate

the probability for switching from the lower (red) to the upper (black) adiabatic curve shown in Supplementary Figure 13. In the given scenario this probability is negligibly small because of the very large non-diagonal coupling element H_{12} (see Eq. S1). The latter is approximately half of the energy difference between the minima on the two adiabatic surfaces. From this it follows that the molecular chemisorbed state (left potential minimum on the red curve) is accessible. However, as becomes obvious when calculating the barrier for the next step in the oxidation reaction (see the top right-hand inset in the figure), the splitting of the O−O bond remains the rate-determining step in this case of an “irreversible" oxidation. In fact, if the O−O bond is broken, it is highly improbable to turn back: it would be necessary to overcome a high energy penalty and to redistribute this energy in vibrational excitations. From Supplementary Figure 13, it can be also seen that, due to the high energy of the excited state at the asymptotic limit, oxygen is released as a neutral molecule.

Supplementary Section 11: Reversible molecular oxidation of Cu_5–$(O_2)_3$

An analysis of the multi-reference wavefunction of the Cu_5–$(O_2)_3$ complex at the molecular chemisorption minimum was carried out first. It revealed that, at the chemisorption minimum, the Cu_5 cluster becomes the carrier of three superoxide O_2^- radical, similarly to the Cu_5–$(O_2)_4$ complex (see Supplementary Section 13). As mentioned in the methods section, the neutral and ionic states characterizing the O_2–$(Cu_5(O_2)_2)$ interaction were calculated in a similar way to that employed in a previous study on the “molecular" oxidation of a reduced $TiO_2(110)$ surface (see Ref. 23). The ionic state, which is the ground state at the chemisorption minimum, is characterized by the strong Coulomb interaction between a negatively charged superoxo O_2^- radical and a positively charged $(Cu_5(O_2)_2)^+$ system and is asymptotically correlated to a separation in charged fragments O_2^- and $(Cu_5(O_2)_2).^+$ In contrast, the neutral state corresponds to the interaction between neutral fragments, and leads to a separation into the O_2 molecule and the $Cu_5(O_2)_2$ complex. This state is the ground state at the physisorption minimum, as shown in Supplementary Figure 14, panel

a. The calculations provided a value of 0.12 eV for the energetic barrier, which is comparable to that published in Ref. 1 (0.09 eV, see Supplementary Figure 13) where only one O_2 molecule was considered for the first step of the oxidation of Cu_5. It is interesting to observe that chemisorbed O_2 molecules are barely affecting the (low) height of the barrier in successive oxidation steps, explaining the resistance to oxidation at lower temperatures and its reversibility at higher temperatures. In contrast, an important collaborative effect is found in regards to the stability of the chemisorption well, which is much deeper (-1.16 eV) in the case of the $Cu_5(O_2)_2$ + O_2 reaction than in first oxidation step of the Cu_5 cluster (see Supplementary Figure 13). However, even considering this collaborative effect, the ionic pair state remains too high in energy to allow a chemical ionization of the Cu_5 cluster. A net charge on the cluster oxide is thus forbidden energetically and consistent with the reversible oxidation observed experimentally.

To ensure that the oxidation is indeed reversible, in addition of discarding the possibility of chemical ionization, it is necessary to ensure that O_2 molecules cannot dissociate. Since the collaborative effect induces a larger stability than a single O_2 molecule, one may wonder if this extra energy allows the O_2 molecule to dissociate on the cluster. Panel **b** of Supplementary Figure 14 clearly shows that it is not the case. The energy required to dissociate O_2 is higher than 4 eV, much larger than the extra stability provided by the collaborative effect.

Summarizing, the application of multireference perturbation theory to the O_2–Cu_5 system[1] and the O_2–($Cu_5(O_2)_2$) complex, has allowed us to reveal that the energy barriers to O_2 dissociation are very high (of a few eV, see Supplementary Figure 14a). Conversely, the energetic barriers to reach the molecular chemisorption states from the physisorption counterparts are very low (ca. 0.1 eV, see Supplementary Figure 14b). This confirms that: (1) the oxidation is expected to be reversible even when several O_2 molecules are chemisorbed; (2) the chemisorption is much more likely than physisorption when several O_2 molecules are involved.

Supplementary Section 12: Molecular chemisorption states of Cu_5–$(O_2)_n$ complexes

In order to consider a larger number of O_2 molecules adsorbed on the Cu_5 cluster, we have applied density functional theory as described in the Methods section. The optimized geometries of Cu_5–$(O_2)_n$ complexes are shown in Supplementary Figure 15, as calculated with the PBE-D3(BJ) approach and the def2-TZVP basis set. The values of the adsorption energies as a function of the number of O_2 molecules are indicated in Supplementary Figure 15 (see also Supplementary Figure 16). The optimization of geometries has been performed using both the def2-SVP and the def2-TZVP basis sets in order to ensure convergence in the values of the structural parameters (see Supplementary Figure 17a). Since minor modifications are found in structural parameters such as Cu−Cu distances when using def2-SVP and def2-TZVP basis sets (see Supplementary Figure 17a), the resulting optimized structures are expected to be rather well converged when using the def2-TZVP basis. Therefore, this basis was used to calculate the frequencies necessary for thermochemistry (see Section 14).

Binding energies E_b are defined as

$$E_b = E_{Cu_5-(O_2)_n} - E_{Cu_5} - n \cdot E_{O_2} \tag{S4}$$

and have been calculated using the def2-TZVP and def2-QZVPP basis sets. Upon augmenting the basis set, binding energies become ca. 0.18 eV lower in average with the largest (def2-QZVPP) basis set, while the inclusion of the Boys-Bernardi counterpoise correction[20] made them ca. 0.22 eV higher. Hence, the values of the binding energies are considered to be also well converged using the latter. The same holds true with the values of the adsorption energies E_{ads} as shown in Supplementary Figure 16, which are defined as

$$E_{ads} = E_{Cu_5-(O_2)_n} - E_{Cu_5-(O_2)_{n-1}} - E_{O_2} \tag{S5}$$

The analysis of Supplementary Figure 15 (see also Supplementary Figure 16) points out the enhanced stability of the Cu_5–$(O_2)_n$ complexes for which the O_2 molecules locate at bridge positions of the Cu_5 cluster. Less stable structures involve the attachment of O_2 molecules to one copper atom only. For example, as can be observed in Supplementary Figure 15, the very small adsorption energy (less than -0.05 eV) of one additional O_2 molecule to the Cu_5–$(O_2)_7$ complex indicates that it becomes physisorbed. The addition of further O_2 molecules involves either positive or very small adsorption energies (ca. 0.1 eV as much), indicating the lack of stability of complexes with $n > 7$.

Notice from Supplementary Figure 17a that the Cu−Cu bond lengths increase in comparison to those of the bare Cu_5 cluster upon adsorption (see also Supplementary Figure 18). According to the atomic spin populations, the O_2 molecules become either superoxo or peroxo species, which is also reflected in the enlargement of the O−O bond lengths (larger than ca. 1.4 Å) upon adsorption from the value for the neutral O_2 molecule (ca. 1.2 Å). As shown in Supplementary Figure 17b, it is necessary to add the dispersion interaction in getting the right structure for the complex bearing the maximum number of O_2 molecules adsorbed on bridge sites (i.e, the Cu_5–$(O_2)_7$ complex). The inclusion of the dispersion is in fact correlated with the enlargement of the Cu−Cu bonds, as necessary to accommodate peroxo and superoxo species with larger O−O bond lengths than for the neutral O_2 molecule.

We also compared adsorption energies obtained at DFT and MP2 levels of theory, finding that the complexes with 3 and 7 O_2 molecules are the most stable at 0 K. For the complex with 7 O_2 molecules, the MP2 adsorption energy was ca. 0.5 eV lower than the DFT value using the def2-SVP basis set. Using the def2-TZVP basis set instead, the energy difference between MP2 and DFT values was also found to be ca. 0.5 eV for the Cu_5–O_2 complex. Considering that the single-point MP2 calculations are performed on top of optimized structures via DFT and not MP2 calculations, energy differences of ca. 0.5 eV are sensible, indicating that the DFT approach is sufficient in getting reasonable values of adsorption and binding energies.

The Cu_5 cluster can be thought as a network in which all atomic nuclei and electrons motions

are collectively correlated. For instance, as can be seen in Supplementary Figure 18a, the Cu_5 cluster adsorbs and loses O_2 molecules by concerted elongations and contractions of the Cu−Cu bonds. The same holds true for the motion of electrons: as illustrated in Supplementary Figure 18b, the electronic charge is collectively shared by all O_2 molecules and mainly located in their π^* orbitals. It is interesting that this collective effect favors the charge transfer from the Cu_5 cluster to the O_2 molecules when the number of O_2 molecules increases. For instance, when only one O_2 is chemisorbed at the bridge adsorption site located at the equatorial plane of the Cu_5 cluster, only a partial charge transfer is observed.[1] On one hand, this partial charge transfer arises from the very favorable overlap of the π^* orbital from the oxygen atoms, located at the equatorial plane of the cluster, with several $d-$type orbitals of the copper atoms. This special orbital from the adsorbed O_2 molecule will be referred to as the $\pi^*(A')$ orbital since it bears A′ symmetry with respect to the equatorial plane of the cluster. As a representative example, the interaction of this $\pi^*(A')$ orbital with one of the d-type orbitals from the copper atoms is depicted in Supplementary Figure 18c. On the other hand, the $\pi^*(A'')$ orbital (which is anti-symmetric with respect to the equatorial plane) barely overlaps with the d-type orbitals and does not contribute to the bonding, as can be seen in the left-hand panel of Supplementary Figure 18c. Importantly, when a second O_2 molecule becomes attached to the Cu_5 cluster at its vortex adsorption site, the whole structure of the d-type orbitals from copper atoms becomes distorted. This distortion does not affect the favorable overlap of the $\pi^*(A')$ orbitals, but it allows a more favorable interaction of the $\pi^*(A'')$ orbitals with the d-type orbitals of the Cu_5 cluster, as shown in the right-hand panel of Supplementary Figure 18c. Since a similar effect occurs not only for the represented orbitals, but also for many of them, the bonding between both the π^* orbitals of the O_2 molecules adsorbed on the bridge sites with several d-type orbitals from the copper atoms allows the oxygen molecules to drain more efficiently electrons from the copper atoms leading to net charge transfers. This effect is then additive for each additional oxygen molecule which becomes adsorbed to the Cu_5 cluster. Notice that the collective effects in the atomic nuclei and electrons motions are possible due to the subnanometer-sized network formed by the $3d$-orbitals of the copper atoms.

Supplementary Section 13: Oxidation states of the copper atoms: multireference theory

To provide measurable predictions, we have assigned oxidation [Cu(0), Cu(I), Cu(II)] states to the copper atoms of each Cu_5–$(O_2)_n$ complex since experimental measurements have provided relative Cu oxidation states at different values of temperature and pressure. Assigned oxidation [Cu(0), Cu(I), and Cu(II)] states for each Cu_5–$(O_2)_n$ complex are indicated in Supplementary Figure 15, as deduced from an analysis of Mulliken charges[32] and atomic spin populations using the Hirshfeld method.[33,34] For the purpose of comparison, this analysis has been realized at both the PBE-D3(BJ) and the Hartree-Fock level of theory.

To provide a more accurate analysis of the the nature of the chemical oxidation states of copper atoms for the most stable Cu_5–$(O_2)_n$ complexes, we have also applied high level multireference *ab initio* theory. It should be stressed that the peroxo or superoxo character of the adsorbed O_2 molecules as well as differential effects in Cu(I) and Cu(II) oxidation states could be assigned even at the HF level. A Hirshfeld analysis of atomic spin populations revealed that a characteristic of the most stable Cu_5–$(O_2)_4$ and Cu_5–$(O_2)_7$ complexes is in bearing a net unpaired electron on the $3d$ orbitals of one ($n = 4$) or three ($n = 7$) copper atoms. This is one of the signatures of the possible occurrence of Cu(II) oxidation states since the electronic configuration of bare copper atoms (i.e., in the Cu(0) state) can be approximated to a first-order as: $[\mathrm{Ar}](3d)^{10}(4s)^1$, with [Ar] denoting the electronic configuration of argon. However, the Hartree-Fock method is still a single-reference approach. To properly account for the open-shell nature of the interacting systems, multireference perturbation theory has been applied. These calculations were computationally very expensive, encompassing hundreds of millions of configuration state functions. Both doublet and quartet spin states were considered, finding them almost degenerate as expected: the total energy is kept almost unperturbed upon the spin-flip of unpaired electrons located on distant superoxo O_2^- radicals (from, e.g., anti-ferromagnetic to ferromagnetic configurations).

Supplementary Section 13.1 Cu_5–$(O_2)_4$

The correlated analysis of spin atomic populations (Hirshfeld analysis) and Mulliken charges of the natural orbitals reveals that the Cu_5–$(O_2)_4$ cluster oxide bears five unpaired electrons when four O_2 molecules are chemisorbed. To describe properly a doublet spin wave-function encompassing five unpaired electrons and estimate the correct charge distribution, it is mandatory to use multireference methods. From the analysis of the multi-reference wave-function, it is clear that all O_2 molecules in the Cu_5–$(O_2)_4$ complex can be characterized as superoxo O_2^- radicals, with a spin of almost unity for each of them and a Mulliken charge of ca. $-0.7\ |e|$. It is known that the Mulliken analysis generally underestimates the ionicity degree of the binding, but remaining globally proportional to the real charge distribution. Since the four oxygen molecules present an unitary spin, it can be assumed that they strip four electrons (one each) to the Cu_5 cluster. The copper atom coordinated with three oxygen atoms (labelled as Cu3 in Supplementary Figure 19) is the atom having a single-occupied $3d$ orbital. Its electronic configuration can be roughly approximated as $[Ar](3d)^9(4s)^0$. Sharing one electron from one $3d$ orbital makes its binding with three oxygen atoms possible. This electronic configuration for a single copper atom would suggest that it presents a Cu(II) oxidation state. However, since it bears the same value of the Mulliken charge as the four O_2 molecules, but of opposite sign, it is clear that its oxidation state is Cu(I). This is due to the ability of the cluster to redistribute the charge towards other copper atoms through a complex binding network formed by the $d-$orbitals. As a consequence of this positive charge delocalization, the other vortex copper (labelled Cu2 in Supplementary Figure 19) bears the same Mulliken charge and can be also assigned with a Cu(I) oxidation state, even if coordinated to just one oxygen atom. The two remaining positive charges are delocalized over the three equatorial copper atoms with an oxidation state which is intermediate between the Cu(0) and Cu(I) states (i.e., approximately +2/3).

The fact that the copper cluster becomes the carrier of four superoxo radicals is also reflected on the spin degeneracy of doublet and quartet spin states due to the small magnetic coupling be-

tween unpaired electrons located in π^* orbitals of distant O_2 molecules. Thus, energy differences below 0.01 eV were found in the the CASPT2 calculations, involving about 250 millions of configuration state functions. The wavefunctions were found to be highly multi-configurational, encompassing ca. 22 configuration state functions with coefficients larger than 0.1 for the doublet spin state. Hence, an analysis of the natural orbitals from such multi-configurational wave-function was mandatory to ensure the identification of the nature of copper oxidation states.

The five singly-occupied orbitals of the system are represented in Supplementary Figure 19. A simple molecular orbital model is capable of explaining the nature of the copper oxidation states. As can be clearly seen from Supplementary Figure 19, one electron is located on a pure π^* orbital of one O_2 molecule (shown at the right-hand panel), with its other π^* orbital being filled (i.e., double occupied). Hence, it is evident that one negative charge is localized on this molecule.

It can be also observed in Supplementary Figure 19 that two unpaired electrons are located in two orbitals which are essentially linear combination of two π^* orbitals from the second and third oxygen molecules, with a small contribution from the fourth (shown in the middle panel). In a first-order approximation, two unpaired electrons which are delocalized on two sites can be thought as one electron on each oxygen molecule, with their other π^* orbitals being filled for both O_2 molecules. Hence, it is clear that each O_2 molecule bears one negative charge as well.

Finally, the two remaining unpaired electrons are located in two molecular orbitals which are combinations between one *d*-orbital of the copper atom labelled as Cu_3 in Supplementary Figure 19 and one π^* orbital from the fourth oxygen molecule. One molecular orbital is bonding and the other one is anti-bonding, with both having a small contamination of the π^* orbital from the third oxygen molecule. In a first-order approximation, the two unpaired electrons are thus located on the fourth oxygen molecule and on the vortex Cu atom coordinated with three oxygen atoms, with the other π^* orbital of this fourth oxygen molecule being filled too. Thus, it is apparent that the fourth O_2 molecule bears one negative charge.

It is noticed that the bare Cu_5 cluster conserves an unpaired electron. However, instead of being delocalized in several *s*-type orbitals as for the isolated cluster, it becomes localized in one

d-type orbital. This qualitative model based on interpretation of the molecular orbitals leads to the conclusion that the Cu_5 cluster should carry four positive charges spread over five copper atoms, giving a mean value of 0.8 $|e|$. This is in agreement with the assignment from the Mulliken population analysis, which predicts two copper atoms having the Cu(I) oxidation state, with two positive charges distributed over three copper atoms located at the equatorial plane.

In order to emphasize the importance of an appropriate multi-reference treatment in characterizing properly the charge distribution of this system, we mention that our DFT calculations using the largest (def2-QZVPP) basis set provided a prediction of the net charge transfer of ca. 1.4 $|e|$ only and no net (almost unity) spin population on copper atoms whatever the complex size be.

Supplementary Section 13.2 Cu_5–$(O_2)_7$

The analysis of the density matrix from the multi-configurational wave-function for the Cu_5–$(O_2)_7$ complex clearly reveals a Cu(II) oxidation state for three copper atoms (labelled as Cu_2, Cu_3, and Cu_5 in Supplementary Figure 20a) while the other two copper atoms can be characterized with the Cu(I) oxidation state (labelled as Cu_1 and Cu_4 in Supplementary Figure 20a). Obviously, copper atoms having higher oxidation states are those coordinated to more oxygen atoms. The adsorbed O_2 molecules can be clearly characterized as either superoxo or peroxo radicals, with one neutral O_2 molecule having been identified as well. As for the Cu_5–$(O_2)_4$ complex, the quartet and doublet spin states were found to be almost degenerate (to within 0.01 eV).

As can be observed in Supplementary Figure 20a, copper atoms in assigned Cu(II) oxidation states are characterized by having, approximately, one single-occupied 3*d* orbital and an unoccupied 4*s* orbital. Actually, the loss of electronic charge from 3*d* (0.8−0.9 $|e|$) and 4*s* (ca. 0.6 $|e|$) orbitals is not unity, when analyzed with the Mulliken analysis. The analysis of spin atomic populations is even more conclusive, predicting the copper atoms in Cu(II) oxidation states as having a spin population close to unity. Moreover, they bear about the same value of the Mulliken charge as the peroxo radicals but opposite sign. However, from Supplementary Figure 20b, an increase of the electronic charge located in *p*-type orbitals can be also observed (0.2−0.4 $|e|$), which is attributed

to a back-donation transfer process from the O_2 molecules to the Cu_5 cluster.

As shown in Supplementary Figure 20c, O_2 molecules adsorbed as superoxo (O_2^-) and peroxo (O_2^{2-}) radicals receive a Mulliken charge donation of ca. 0.6 and 1.1 $|e|$, respectively. This excess electronic charge is accommodated in atomic p-type orbitals. Our assignment is confirmed from the spin atomic population analysis using the Hirshfeld method. Notice that the electronic population of s-type orbitals decrease by ca. 0.1 $|e|$ per oxygen atom. Hence, a back-donation transfer of electronic charge is predicted from s-type orbitals of adsorbed O_2 species to p-type orbitals of the Cu_5 cluster (see Supplementary Figure 20b). The net charge donation from the Cu_5 cluster, as estimated through the Mulliken populations, is close to 5 $|e|$ in total. Once again, this value is smaller than expected from the formation of 4 superoxo and 2 peroxo radicals (i.e., 8 $|e|$). Besides the well-known underestimation of electronic charge transfer using the Mulliken analysis, there is also a clear back donation from the O_2 molecules to the Cu_5 cluster (ca. 1.4 $|e|$).

The multi-configuration nature of the wavefunction for the Cu_5–$(O_2)_7$ complex is also worth stressing, encompassing ca. 20 configurations with coefficients larger than 0.05. Remarkably, the Hartree-Fock method is already capable of providing correct values of the oxidation states for copper atoms via the Hirshfeld analysis of their spin atomic populations. Thus, the three copper atoms highlighted in red in Supplementary Figure 20a carry spins close to unity.

Supplementary Section 14: Helmholtz free energies of formation and phase diagram of Cu_5–$(O_2)_n$ complexes

At given temperature (T) and partial oxygen pressure (p), the relative stability of complexes Cu_5–$(O_2)_n$ bearing an arbitrary number of absorbed molecules (n) can be determined by calculating the Helmholtz free energy of formation[35–38] (also named potential ω in Ref. 36):

$$\Delta H_f(p,T) = F_{Cu_5-(O_2)_n}(T) - F_{Cu_5}(T) - n \cdot \mu_{O_2}(p,T) \tag{S6}$$

where $F_{Cu_5-(O_2)_n}$ and F_{Cu_5} are the Helmholtz free energies of the $Cu_5-(O_2)_n$ complex and the bare Cu_5 cluster, and μ_{O_2} is the chemical potential of molecular oxygen. This definition is equivalent to the potential ω, as stated in Ref. 36:

$$\omega(T,\mu_{O_2},n) = \Delta E_{F,\mathrm{corr}}(T) - T\cdot s_{Cu_5-(O_2)_n}(T) + T\cdot s_{Cu_5}(T) - n\cdot\mu_{O_2}(p,T). \tag{S7}$$

A (p,T)-phase diagram for Cu_5–$(O_2)_n$ complexes can be constructed on the basis of the potential ω. Assuming a constant number N of Cu_5 clusters but arbitrary amounts of molecular oxygen in the system, $\omega(T,\mu_{O_2},n)$, is defined as the grand potential Ω divided by N, which is a function of the temperature T, the chemical potential of molecular oxygen μ_{O_2}, and the number of adsorbed O_2 molecules n (see Eq. S4). In a first approximation, the Cu_5 clusters are treated as fully immobilized on support coupled to a heat bath of temperature T and an infinite reservoir of O_2 gas at pressure p. Under these idealized circumstances, the so defined thermodynamic potential $\omega(T,\mu_{O_2},n)$ will become minimal at thermodynamic equilibrium. A dependence on O_2 pressure enters via $\mu_{O_2}(p,T)$, the chemical potential of molecular oxygen.

From this, the number n of adsorbed O_2 molecules which minimizes ω for a specified temperature and a given oxygen pressure can be obtained from Eq. S4 as follows. $\Delta E_{F,\mathrm{corr}}$, the first term on the right-hand side, corresponds to the formation energy of Cu_5–$(O_2)_n$ defined as the difference

$$\Delta E_{F,\mathrm{corr}}(T) = E_{Cu_5-(O_2)_n} - E_{Cu_5} - n\cdot E_{O_2} + E_{\mathrm{corr}}(T) \tag{S8}$$

In this equation, $E_{Cu_5-(O_2)_n}$ and E_{Cu_5} denote the DFT energies of the oxygen-covered and pure cluster, respectively, and E_{O_2} is the DFT energy of molecular oxygen. They were obtained with the PBE-D3(BJ) functional using the def2-QZVPP basis set, and including a correction for the basis set superposition error. The last term in Eq. S5, E_{corr}, was introduced to account for the zero-point energy, the thermal vibrational contribution (i.e., as coming from the population of excited vibrational states at a given temperature) as well as to account for thermal rotational, and translational terms. All these corrections were taken from the thermochemistry output of ORCA.[18]

The uncorrected formation energies are plotted in the left-hand panel of Supplementary Figure 21b. The graph shows an approximate linear dependence on the particle number at first, but is also indicating pronounced oxygen interaction effects occurring for higher loads.

The next term on the right-hand side of Eq. S4 introduces a correction with respect to the entropy $s_{Cu_5-(O_2)_n}$ of the cluster. Assuming immobilized copper particles, only vibration and electronic excitation or degeneracy can contribute to the entropy. Vibrational contributions (within the harmonic oscillator approximation) have been also taken from the thermochemistry output of ORCA[18] for temperatures from room temperature (298.15 K) to 773 K. Entropy contributions due to spin multiplicity are automatically included, while contributions due to electronic excitation can be fully neglected at the given temperatures.

We have also ensured the validity of the harmonic approximation for determining the vibrational contributions to the Helmholtz free energies. On one hand, considering Cu_2 as a model system and NIST[39] data values of spectroscopic constants, the anharmonic contribution to the total vibrational energy stays below 2% even at 1000 K. If the potential energy curve of the Cu_2 dimer is first calculated, using the same computational setup as for the Cu_5 cluster, and the exact vibrational energy levels supported by the potential are next determined, the anharmoninc contribution stays below 2.3% of the total vibrational energy term. On the other hand, electronic energy and entropy terms are mainly contributing to the free energies, and not the vibrational contributions. In order to better illustrate these features, we have recalculated the phase diagrams, both removing the whole vibrational contribution, and removing just a 10% of it (as an upper limit for the correction of the anharmonic contribution). As can be observed in Supplementary Figure 22, the phase diagrams are indistinguishable when the (over-)correction for the anharmonic contribution is accounted for.

The last term on the right side of Eq. S4 is the chemical potential μ_{O_2} of molecular oxygen multiplied by the number n of adsorbed molecules. It introduces the pressure dependence and is of the same magnitude as $\Delta E_{F,\mathrm{corr}}$. We write the chemical potential of molecular oxygen as[40]

$$\mu_{O_2}(p,T) = \Delta h_{O_2}(p_0,T) - T \cdot s_{O_2}(p_0,T) + R \cdot T \ln\left(\frac{p}{p_0}\right), \tag{S9}$$

where the pressure enters through the ratio p/p_0, with the reference oxygen pressure p_0 set to 1 atm (ca. 1033 mbar). The change of enthalpy is given by $\Delta h_{O_2} = h(p_0,T) - h(p_0,T=0\,K)$. For maximum accuracy we take the values for h_{O_2} and s_{O_2} from the NIST database.[41,42]

The ω potential is represented in Supplementary Figure 21a for selected sets of (p,T) conditions, including those accessible in the experiment. With all terms of Eq. S4 defined we can now calculate $\omega(p,T,n)$ for the experimentally relevant range of $T = 298$ (room temperature) to 773 K and $p = 1$ atm (1033 mbar) to 10^{-10} mbar and determine the phase of lowest energy for each variable pair (p,T). The resulting phase diagram is given in the right-hand panel of Supplementary Figure 21b. It can be observed that the system is switching between 473 and 673 K. Overall, the phase diagram predicts that complexes with 7 and 4 O_2 molecules as the most stable species at atmospheric pressure and 0.15 mbar, respectively. As in the phase diagram, it can be clearly observed from Supplementary Figure 21a that the Cu_5–$(O_2)_7$ complex is the most stable configuration at standard conditions of temperature and pressure, while the smaller complex Cu_5–$(O_2)_4$ becomes the most stable upon increasing the temperature and decreasing the pressure.

Copper oxide complexes involving the dissociation of O_2 have also been considered in this work. Depending on the size and temperature, complexes with $5 \leq n \leq 9$ and two dissociated O_2 molecules have a Helmholtz free energy of formation in between 2.2 and 3.5 eV below the non-dissociated counterparts. Although the O_2 dissociated complexes would be the “thermodynamic products", the energy barriers are too high (above 4 eV, see Supplementary Figure 2b) for being over-passed at the temperatures used in the experiment (from RT up to 773 K). The formation of O_2 dissociated products would be then thermodynamically allowed but kinetically forbidden.

Supplementary Section 15: Comparison between theory and experiment

In order to compare with experimental results, we have calculated the normalized distributions of the oxidation states at different conditions of temperature and pressure. To this end, we performed

a Boltzmann-weighted average of the Helmholtz free energies of formation for each complex and their associated distributions of oxidation states. The Boltzmann-weighted averages are presented in Supplementary Table 2. Supplementary Figure 23 presents a chart diagram and a Table with a summary of the theoretically and experimentally determined percentage values of Cu(0), Cu(I), and Cu(II) oxidation states at different thermodynamic conditions.

Starting at **atmospheric pressure and room temperature (RT)**, it can be seen from Supplementary Table 2 that the normalized fraction distribution is clearly peaked at the oxidation state Cu(II). In fact, as shown in Supplementary Figure 21, the Cu_5–$(O_2)_7$ complex is predicted to be the most stable at this (T,p) condition, with most of the copper atoms bearing the oxidation state Cu(II) (see Supplementary Figure 15). This outcome is predicted at both DFT and multireference *ab initio* levels of theory (see Supplementary Figure 20). As clearly shown in Supplementary Figure 23, the estimated normalized fractions are consistent with the experimental measurements, providing a majority Cu(II) component at RT (see Figure 2). Upon heating to 473 K, the phase diagram clearly shows that the Cu_5–$(O_2)_7$ complex is still the most stable (see Supplementary Figure 21b), with the Boltzmann average of oxidation states still indicating a major fraction for the Cu(II) oxidation state (see Supplementary Table 2). This is also consistent with the experimental measurements at atmospheric pressure when heating (see Figure 2 and Supplementary Figure 23). At temperatures higher than 473 K, the Cu_5–$(O_2)_7$ complex loses molecules and, as can be observed from Supplementary Figure 21a, the smaller Cu_5–$(O_2)_3$ and Cu_5–$(O_2)_4$ systems stand by as the most stable, bearing very similar Helmholtz free energies of formation.

For higher temperatures (i.e., 673 K), the HOPG-supported Cu_5 clusters aggregate so that the experimental measurements (see Figure 2) not correspond to the genuine Cu_5 cluster and can not be compared with theory. This fusion process occurs at atmospheric pressure but not at lower pressures (i.e., 0.15 mbar) since, at atmospheric pressure, the concentration of Cu_5 clusters has to be much higher.

When the oxygen pressure is lowered from 1 atm to **0.15 mbar**, the normalized fraction distribution (see Supplementary Table 2) is still peaked at Cu(II) at room temperature. However, upon

heating up to 373 K, the larger complexes lose O_2 molecules, and the oxidation states of the smaller Cu_5–$(O_2)_3$ and Cu_5–$(O_2)_4$ complexes become dominant in the distribution so that the normalized fraction distribution gets peaked at the Cu(I) oxidation state.

At 673 K and 0.15 mbar, the normalized fraction is very similar to that measured experimentally, with the Cu(I) oxidation state being clearly the dominant one, and quantitatively, the agreement between theoretical and experimental values is remarkable (Figure 5 and Supplementary Figure 23). Note that the percentage differences between the theoretical values obtained with the average oxidation states estimated from DFT or *ab initio* calculations are up to 20% as large. This value (20%) is considered to be indicative of the (minimum) uncertainty percentage from the theoretically determined fractions.

At 673 K, if the pressure is lowered from 0.15 mbar towards the **HV** condition, the largest normalized fraction distribution is associated to the Cu(0) oxidation state because of the detachment of most of the O_2 molecules from the clusters. Accordingly, the experimentally measured and theoretically predicted normalized fraction gets peaked at Cu(0) (see Figures 3 and 5, and Supplementary Figure 23). This outcome is directly related to the concept of reversible molecular oxidation, with the Cu_5 cluster recovering the Cu(0) state upon desorption of the O_2 molecules.

From the phase-diagram (see Supplementary Figure 21b), it is also clearly apparent that the complex with 7 O_2 molecules is the most stable at **RT and atmospheric pressure** and, then, the Cu(II) oxidation state becomes the major component (see Supplementary Figure 20). Upon heating to about 473 K, the Cu_5 cluster loses O_2 molecules and the complex with 4 O_2 stands out as the most stable, corresponding to the Cu(I) oxidation state. Further lowering of the oxygen pressure makes the copper cluster lose all its O_2 molecules so that the bare Cu_5 cluster is predicted to be the most stable. Consequently, the Cu(0) oxidation state becomes the major component.

From Supplementary Figure 21b and Supplementary Figure 23, it can be observed that, at thermodynamics equilibrium at **RT and HV**, the smaller Cu_5–$(O_2)_4$ complex become the most stable, and then, the fraction associated to the Cu(I) oxidation state is the largest (ca. 0.7, see Supplementary Table 2 and Supplementary Figure 21b). However, the normalized fraction is peaked at Cu(0)

from experimental measurements starting at **RT and HV** (see Figure 3). This highlights that, at this condition, reactivity is dominated by the kinetics and bimolecular collisions and, within the adopted adiabatic approach, the existence of energy barriers between physisorption and chemisorption states must be taken into consideration. As shown in Supplementary Figure 14a (see also Ref. 1), a small energy barrier (ca. 0.1 eV) is predicted for a single O_2 molecule in going from the physisorption to the molecular chemisorption minima so that the Cu_5–$(O_2)_3$ complex is formed. This barrier is large enough to limit accessibility at RT: assuming a Boltzmann distribution of velocities, less than 20% of the O_2 molecules would have enough kinetic energy to overpass the energy barrier so that most of the O_2 molecules would remain trapped at the physisorption state.[2] Obviously, the fraction of O_2 molecules trapped at the physisorption state would not contribute to the Cu(I) fraction as no electron transfer may occur. The probability of trapping at the physisorption state is therefore related to the electron hopping probability. Switching to a diabatic approach, an estimate of the latter can be obtained by applying the non-adiabatic Landau-Zener model to the $Cu_5(O_2)_2$–O_2 collision as the model system (see Supplementary Section 9.1 for the details). The two-dimensional (2D) potential energy surfaces of physisorption and molecular chemisorption states (ionic and neutral states in the diabatic representation) are shown in Supplementary Figure 14 (panel c). The fractions of the oxidation states [75% [Cu(0)], 21% [Cu(I)], 4% [Cu(II)] resulting for the collision at RT are very close to both the theoretical values using the adiabatic scheme[2] as well as the experimentally determined values presented in Supplementary Figure 23 [87% [Cu(0)], 10% [Cu(I)], 3% [Cu(II)] .

The reversibility of the “molecular" oxidation process is reconfirmed by additional experimental measurements, performed at 0.15 mbar, and varying the temperature in the range between 298 K (RT) and 473 K: as shown in Supplementary Figure 23, the normalized distribution of oxidation states is peaked at Cu(I). Upon heating to 373, 523, and 473 K, the fraction of the Cu(0) state becomes very similar to that of the Cu(I) state instead. This process is attributed to the desorption of part of the O_2 molecules from the chemisorption minima via exit channels leading to neutral fragments upon heating. Note that the distribution becomes, once again, peaked at Cu(I) in exper-

imental observations at 0.15 mbar and 673 K (see Supplementary Figure 23). This is consistent with the theoretical calculations since, at the thermodynamic equilibrium, the phase of the Cu_5–$(O_2)_4$ complex, and then the dominance of the Cu(I) state, is predicted at 0.15 mbar from $T = 450$ up to above 673 K (see Supplementary Section 14).

References

(1) Zanchet, A.; López-Caballero, P.; Mitrushchenkov, A. O.; Buceta, D.; López-Quintela, M. A.; Hauser, A. W.; de Lara-Castells, M. P. On the stability of Cu_5 catalysts in air using multireference perturbation theory. *J. Phys. Chem. C* **2019**, *123*, 27064–27072.

(2) The probability of trapping of O_2 reactant species at the physisorption state has been estimated by considering a Maxwell-Boltzmann distribution of their velocities. In this way, the fraction of O_2 molecules with kinetic energy bellow the energy barrier between physisorption and chemisorption states (ca. 0.1 eV) has been calculated (referred to as P). Finally, the fraction of Cu(I) and Cu(II) oxidation states, as arising from O_2 molecules at the chemisorption minima, has been simply multiplied by P (i.e., considering only the O_2 molecules having overpassed the energy barrier of 0.1 eV).

(3) Hill, J.; Royce, D.; Fadley, C.; Wagner, L.; Grunthaner, F. Properties of oxidized silicon as determined by angular-dependent X-ray photoelectron spectroscopy. *Chem. Phys. Lett.* **1976**, *44*, 225 – 231.

(4) Gonzalez, R. C.; Woods, R. E.; Eddins, S. L. *Digital Image processing using MATLAB*, 2nd ed.; Gatesmark Pub: S.I., 2009.

(5) Matthew, J. Surface analysis by Auger and x-ray photoelectron spectroscopy. D. Briggs and J. T. Grant (eds). IMPublications, Chichester, UK and SurfaceSpectra, Manchester, UK, 2003. 900 pp., ISBN 1-901019-04-7, 900 pp. *Surf. Interface Anal.* **2004**, *36*, 1647–1647.

(6) Zhang, R.; McEwen, J.-S. Local environment sensitivity of the Cu K-Edge XANES features in Cu-SSZ-13: Analysis from first-principles. *J. Phys. Chem. Lett.* **2018**, *9*, 3035–3042.

(7) Eren, B.; Heine, C.; Bluhm, H.; Somorjai, G. A.; Salmeron, M. Catalyst chemical state during CO oxidation reaction on Cu(111) studied with ambient-pressure X-ray photoelectron spectroscopy and near edge X-ray adsorption fine structure spectroscopy. *J. Am. Chem. Soc.* **2015**, *137*, 11186–11190.

(8) Grioni, M.; Goedkoop, J. B.; Schoorl, R.; de Groot, F. M. F.; Fuggle, J. C.; Schäfers, F.; Koch, E. E.; Rossi, G.; Esteva, J.-M.; Karnatak, R. C. Studies of copper valence states with Cu L_3-edge x-ray-absorption spectroscopy. *Phys. Rev. B* **1989**, *39*, 1541–1545.

(9) de Lara-Castells, M. P.; Hauser, A. W.; Ramallo-López, J. M.; Buceta, D.; Giovanetti, L. J.; López-Quintela, M. A.; Requejo, F. G. Increasing the optical response of TiO_2 and extending it into the visible region through surface activation with highly stable Cu_5 clusters. *J. Mater. Chem. A* **2019**, *7*, 7489–7500.

(10) Grimme, S.; Ehrlich, S.; Goerigk, L. Effect of the damping function in dispersion corrected density functional theory. *J. Comp. Chem.* **2011**, *32*, 1456–1465.

(11) Grimme, S.; Antony, J.; Ehrlich, S.; Krieg, H. A consistent and accurate ab initio parametrization of Density Functional Dispersion correction (DFT-D) for the 94 elements H-Pu. *J. Chem. Phys.* **2010**, *132*, 154104.

(12) de Lara-Castells, M. P.; Mitrushchenkov, A. O.; Stoll, H. Combining density functional and incremental post-Hartree-Fock approaches for van der Waals dominated adsorbate-surface interactions: Ag_2/graphene. *J. Chem. Phys.* **2015**, *143*, 102804.

(13) de Lara-Castells, M. P.; Bartolomei, M.; Mitrushchenkov, A. O.; Stoll, H. Transferability and accuracy by combining dispersionless density functional and incremental post-Hartree-Fock theories: noble gases adsorption on coronene/graphene/graphite surfaces. *J. Chem. Phys.* **2015**, *143*, 194701.

(14) Bader, R. F. W. A quantum theory of molecular structure and its applications. *Chem. Rev.* **1991**, *91*, 893–928.

(15) Celani, P.; Werner, H.-J. Multireference perturbation theory for large restricted and selected active space reference wave functions. *J. Chem. Phys.* **2000**, *112*, 5546–5557.

(16) de Lara-Castells, M. P.; Cabrillo, C.; Micha, D. A.; Mitrushchenkov, A. O.; Vazhappilly, T. Ab initio design of light absorption through silver atomic cluster decoration of TiO_2. *Phys. Chem. Chem. Phys.* **2018**, *20*, 19110–19119.

(17) López-Caballero, P.; Ramallo-López, J. M.; Giovanetti, L. J.; Buceta, D.; Miret-Artés, S.; López-Quintela, M. A.; Requejo, F. G.; de Lara-Castells, M. P. Exploring the properties of Ag_5–TiO_2 interfaces: stable surface polaron formation, UV-Vis optical response, and CO_2 photoactivation. *J. Mater. Chem. A* **2020**, *8*, 6842–6853.

(18) Neese, F. Software update: the ORCA program system, version 4.0. *Wiley Interdiscip. Rev.: Comput. Mol. Sci.* **2018**, *8*, e1327.

(19) Weigend, F.; Ahlrichs, R. Balanced basis sets of split valence, triple zeta valence and quadruple zeta valence quality for H to Rn: Design and assessment of accuracy. *Phys. Chem. Chem. Phys.* **2005**, *7*, 3297–3305.

(20) Boys, S.; Bernardi, F. The calculation of small molecular interactions by the differences of separate total energies. Some procedures with reduced errors. *Mol. Phys.* **1970**, *19*, 553–566.

(21) Werner, H. J.; Knowles, P. J.; Knizia, G.; Manby, F. R.; Schütz, M.; Celani, P.; Korona, T.; Lindh, R.; Mitrushchenkov, A. O.; Rauhut, G.; et al., MOLPRO, the most recent version, a package of *ab initio* programs, see http://www.molpro.net.

(22) de Lara-Castells, M. P.; Krause, J. L. Theoretical study of the UV-induced desorption of molecular oxygen from the reduced TiO_2(110) Surface. *J. Chem. Phys.* **2003**, *118*, 5098–5105.

(23) de Lara-Castells, M. P.; Mitrushchenkov, A. O.; Roncero, O.; Krause, J. L. Adsorption and nonadiabatic processes in the photodesorption of molecular oxygen from the reduced TiO_2(110) surface. *Isr. J. Chem.* **2005**, *45*, 59–76.

(24) Kreplin, D. A.; Knowles, P. J.; Werner, H.-J. Second-order MCSCF optimization revisited. I. Improved algorithms for fast and robust second-order CASSCF convergence. *J. Chem. Phys.* **2019**, *150*, 194106.

(25) Werner, H.-J. et al. The Molpro quantum chemistry package. *J. Chem. Phys.* **2020**, *152*, 144107.

(26) Woon, D. E.; Dunning, Jr., T. H. Gaussian basis sets for use in correlated molecular calculations. Calculation of static electrical response properties. *J. Chem. Phys.* **1994**, *100*, 2975–2988.

(27) Figgen, D.; Rauhut, G.; Dolg, M.; Stoll, H. Energy-consistent pseudopotentials for group 11 and 12 Atoms: Adjustment to multi-configuration Dirac-Hartree-Fock data. *Chem. Phys.* **2005**, *311*, 227–244, Relativistic effects in heavy-element chemistry and physics. In Memoriam Bernd A. Hess (1954–2004).

(28) Mitrushenkov, A. O.; Palmieri, P.; Puzzarini, C.; Tarroni, R. Numerical techniques for the evaluation of non-adiabatic interactions and the generation of quasi-diabatic potential energy surfaces using configuration interaction methods. *Mol. Phys.* **2000**, *98*, 1677–1690.

(29) de Lara-Castells, M. P.; Hauser, A. W.; Mitrushchenkov, A. O. Ab initio confirmation of a harpoon-type electron transfer in a helium droplet. *J. Phys. Chem. Lett.* **2017**, *8*, 4284–4288.

(30) Landau, L. D. Zur Theorie der Energieubertragung. II. *Phys. Z. Sowjetunion* **1932**, *2*, 46–51.

(31) Zener, C. Non-Adiabatic Crossing of Energy Levels. *Proc. R. Soc. London, Ser. A* **1932**, *137*, 696–702.

(32) Mulliken, R. S. Criteria for the construction of good self-consistent-field molecular orbital wave functions, and the significance of LCAO-MO population analysis. *J. Chem. Phys.* **1962**, *36*, 3428–3439.

(33) Hirshfeld, F. L. Bonded-atom fragments for describing molecular charge densities. *Theor. Chim. Acta* **1977**, *44*, 129–138.

(34) Bultinck, P.; Van Alsenoy, C.; Ayers, P. W.; Carbó-Dorca, R. Critical analysis and extension of the Hirshfeld atoms in molecules. *J. Chem. Phys.* **2007**, *126*, 144111.

(35) Yu, X.; Oganov, A. R.; Zhu, Q.; Qi, F.; Qian, G. The stability and unexpected chemistry of oxide clusters. *Phys. Chem. Chem. Phys.* **2018**, *20*, 30437–30444.

(36) Hauser, A. W.; Gomes, J.; Bajdich, M.; Head-Gordon, M.; Bell, A. T. Subnanometer-sized Pt/Sn alloy cluster catalysts for the dehydrogenation of linear alkanes. *Phys. Chem. Chem. Phys.* **2013**, *15*, 20727–20734.

(37) Bhattacharya, S.; Levchenko, S. V.; Ghiringhelli, L. M.; Scheffler, M. Stability and metastability of clusters in a reactive atmosphere: Theoretical evidence for unexpected stoichiometries of $Mg_M\mathbf{O}_x$. *Phys. Rev. Lett.* **2013**, *111*, 135501.

(38) Xu, Y.; Shelton, W. A.; Schneider, W. F. Thermodynamic equilibrium compositions, structures, and reaction energies of Pt_xO_y ($x = 1-3$) clusters predicted from first principles. *J. Phys. Chem. B* **2006**, *110*, 16591–16599.

(39) P. J. Linstrom and W. G. Mallard, Eds., NIST Chemistry WebBook, NIST standard reference database number 69, National Institute of Standards and Technology, Gaithersburg MD, 20899, https://doi.org/10.18434/T4D303, (retrieved December 02, 2020).

(40) Persson, K. A.; Waldwick, B.; Lazic, P.; Ceder, G. Prediction of solid-aqueous equilibria: Scheme to combine first-principles calculations of solids with experimental aqueous states. *Phys. Rev. B* **2012**, *85*, 235438.

(41) P. J. Linstrom and W. G. Mallard, Eds., NIST Chemistry WebBook, NIST standard reference database number 69, National Institute of Standards and Technology, Gaithersburg MD, 20899, https://doi.org/10.18434/T4D303, (retrieved November 26, 2019).

(42) Chase, M. W., Jr., NIST-JANAF Themochemical Tables, Fourth Edition, J. Phys. Chem. Ref. Data, Monograph 9, 1998, 1-1951.